Enhancing PET Images by Means of Bates' Blind Deconvolution

Daisuke OKANO[1†]
Souichiro AOGAKI[1]
Fujio TAKEUTCHI[2]
F. Masafumi TOYAMA[1]

[1]Department of Information and Communication Sciences,
Kyoto Sangyo University
[2]Department of Computer Sciences,
Kyoto Sangyo University
Kyoto 603-8555, Japan

Abstract

Positron emission tomography (PET) is an innovative inspection method for early detection and treatment of cancer etc. The practical use of PET is rapidly advanced in recent years. However, the resolution of the PET images is yet to be improved for both purposes. There are two elements in improving the resolution of the PET images. One is the gamma-ray detection-system, and the other is the image processing system. The purpose of this work is to examine whether or not the improvement of the resolution of the PET images can be achieved by image-restoration technique. For this purpose, we explore Bates' blind deconvolution that is regarded as an extended method of the one-dimensional signal conditioning with zero-values of signals. We developed some new technical tools for that study and show how they are useful. We present a PET image that we successfully enhanced by means of Bates' blind deconvolution.

1. Introduction

The practical use of positron emission tomography (PET) is advanced in recent years[1)]. The PET is one of the medical treatment inspection methods of discovering focuses by detecting the positions of radioactive sources. By a medicine injected into the inside of the body, positrons are emitted at a focus, where a large amount of energy is consumed. Then, pairs of two photons (gamma rays) are emitted into opposite directions by pair annihilations of electrons and positrons at the focus. The radiation sources are specified by measuring the pairs of two photons simultaneously with detectors placed on the surroundings of the specimen. By analyzing the radiation sources the image of the focus is obtained.

The PET is being used for actual medical treatments as stated above. However, at present the resolution of the PET images is not high enough for the diagnosis use. There are

† present address: 日立製作所ディフェンスシステム事業部, 情報システム本部空間情報システム設計部

two elements in achieving a high resolution of the PET images. One is the correlation-detection system of gamma rays, and another is the image-processing system. The purpose of this work is to examine whether or not the resolution of the PET images can be improved by image-restoration.

There are various methods for the image-restoration processing. They are, for example, the image-restoration using windows[2], the frequency-response analysis and etc.[3]. The aim of this work is to restore the PET images for the medical treatment. We have no advance knowledge about blur-images that may be convoluted in observed PET images. Hence, the image restoration that we have to deal with in this work is the so-called "blind deconvolution". An advanced method in this blind deconvolution is the zero-sheet method. This is regarded as an extended method of the one-dimensional signal conditioning with zero-values of signals. The zero-sheet method is mathematically elegant and innovative in the sense that it enables us to remove blur-elements analytically. Bates presented the basic idea of the zero-sheet method in 1987[4]. However, it did not become popular because it is based on unfamiliar mathematics of the z-transform.

In this work, we examine the blind deconvolution of the PET images using the Bates' zero-sheet method. As we have mentioned, the zero-sheet method is not a popular image processing. Therefore, there are a lot of technical subjects that should be solved for the practical use of the zero-sheet method. Further, because the zero-sheet method is the image-processing method that needs big computational complexity, we should develop useful new techniques with which image-restoration can be performed almost automatically. An essential problem in the zero-sheet method is how we separate zero-sheets of blur-images from those of original images. At present, a versatile method for this has not yet been established. In this work, we developed some useful techniques for the practical use of the zero-sheet method.

In Sec. 2 we give an overview of the basic algorithm of the Bates' blind deconvolution. In Sec. 3 we demonstrate the Bates' blind deconvolution using a model image. This is also a test of the Bates' method. In Sec. 4, we present some new techniques that we developed in the present work. We show how they are useful for the Bates' blind deconvolution. In Sec. 5, we present our result of the image-restoration of an actual PET image. A summary is given in Sec. 6.

2. Overview of the Bates' blind deconvolution

In this section we give an overview of the basic idea of Bates' blind decovolution. This method is based on the so-called zero-value problem. This method is regarded as an extension of the one-dimensional signal conditioning with zero-values of signals.

An observed image of the size $M' \times N'$ is expressed by a real function $g(x, y)$, where x and y are coordinates of the image, i.e., $x = 0, 1, 2, \ldots, M' - 1$ and $y = 0, 1, 2, \ldots, N' - 1$. The z-transform of $g(x, y)$ is written as

$$G(u, v) = \frac{1}{M'N'} \sum_{x=0}^{M'-1} \sum_{y=0}^{N'-1} g(x, y) u^x v^y, \tag{2.1}$$

where u and v are complex variables. We call the function $G(u, v)$ a representation of the observed image in $u - v$ space (z-space). If we take u and v as $u = e^{-2\pi i\xi/M'}$ and $v = e^{-2\pi i\eta/N'}$, Eq. (2.1) is just the two-dimensional Fourier transform. In this sense, the z-transform is a generalization of the Fourier transform. Suppose that the observed image $g(x, y)$ is given as a convolution of an original image $f(x, y)$ of the size $M \times N$ and a blur-image $h(x, y)$ of the size $m \times n$. The blur-image $h(x, y)$ deteriorates the original image $f(x, y)$. In this situation, $G(u, v)$ can be written as

$$G(u, v) = \frac{1}{M'N'} \sum_{x=0}^{M'-1} \sum_{y=0}^{N'-1} g(x, y) u^x v^y = F(u, v) H(u, v), \tag{2.2}$$

where

$$F(u, v) = \frac{1}{MN} \sum_{x=0}^{M-1} \sum_{y=0}^{N-1} f(x, y) u^x v^y \tag{2.3}$$

and

$$H(u, v) = \frac{1}{mn} \sum_{x=0}^{m-1} \sum_{y=0}^{n-1} h(x, y) u^x v^y. \tag{2.4}$$

Note that $M' = M + m - 1$ and $N' = N + n - 1$. Thus, in $u - v$ space the observed image is given as a product of the original image and the blur-image.

We express the complex variable u in Eq. (2.1) as

$$u = \rho_u \exp(i\phi_u), \tag{2.5}$$

where ρ_u and ϕ_u are real parameters ($\rho_u \neq 0$, $0 \leq \phi_u \leq 2\pi$). For a fixed ρ_u and a ϕ_u, $G(u = \rho_u e^{i\phi_u}, v)$ of Eq. (2.1) is a polynomial of v. Therefore, we can express $G(u = \rho_u e^{i\phi_u}, v)$ as a factorization with the roots (zero-values) $\beta_k (k = 1, \ldots, N'')$ of $G(u = \rho_u e^{i\phi_u}, v) = 0$, i.e.,

$$G(u = \rho_u e^{i\phi_u}, v) = \frac{1}{M'N'} \sum_{x=0}^{M'-1} \sum_{y=0}^{N'-1} g(x, y) (\rho_u e^{i\phi_u})^x v^y = A_u \prod_{k=1}^{N''} (v - \beta_k), \quad (N'' \leq N' - 1), \tag{2.6}$$

where $\beta_k = \beta_k(\rho_u, \phi_u)$ and $A_\mu = A_\mu(\rho_u, \phi_u)$. Similarly, if we express v as

$$v = \rho_v \exp(i\phi_v), \tag{2.7}$$

then G of Eq. (2.1) is also written as

$$G(u, v = \rho_v e^{i\phi_v}) = \sum_{x=0}^{M'-1} \sum_{y=0}^{N'-1} g(x, y) u^x (\rho_v e^{i\phi_v})^y = A_v \prod_{k=1}^{M''} (v - \gamma_k), \quad (M'' \leq M' - 1) \tag{2.8}$$

where $\gamma_k = \gamma_k(\rho_v, \phi_v)$ $(k = 1, \ldots, M'')$ are the roots of $G(u, v = \rho_v e^{i\phi_v}) = 0$ and $A_v = A_v(\rho_v, \phi_v)$. Thus, it seems that in $u - v$ space the observed image G can be reconstructed by either zero-values β_k's or γ_k's. However, the factors A_u and A_v cannot be determined by zero-values β_k or γ_k. To reconstruct the observed image by using β_k's or γ_k's, we have to adjust the con-

stants A_u and A_v using both Eqs. (2.6) and (2.8).

As seen from Eq. (2.2), the factors $v - \beta_k$ ($k = 1,\ldots, N'$) in Eq. (2.6) consist of those of $F(u = \rho_u e^{i\phi_u}, v)$ and $H(u = \rho_u e^{i\phi_u}, v)$. Therefore, by judging which factors of $v - \beta_k$ ($k = 1, \ldots, N'$) in Eq. (2.6) belong to those of $H(u = \rho_u e^{i\phi_u}, v)$, in $u - v$ space we can get rid of blur-images from the observed image. This can be performed by classifying β_k's into some groups. The classification of β_k's is done by changing the parameters ρ_u and ϕ_u. When we vary ϕ_u from 0 to 2π for a fixed ρ_u, β_k's compose some closed curves. In this way, β_k's are classified into some groups. However, there is no unique way to judge the zero-values of the blur-images. Small image elements can be the candidates for the blur-images.

We explain this situation with a toy image. The toy image is defined by

$$\begin{bmatrix} g(3,0) & g(3,1) & g(3,2) & g(3,3) \\ g(2,0) & g(2,1) & g(2,2) & g(2,3) \\ g(1,0) & g(1,1) & g(1,2) & g(1,3) \\ g(0,0) & g(0,1) & g(0,2) & g(0,3) \end{bmatrix} = \begin{bmatrix} f & 0 & 0 & 0 \\ 0 & 0 & f & 0 \\ 0 & f & 0 & 0 \\ 0 & 0 & 0 & f \end{bmatrix}, \tag{2.9}$$

where $0 < f \leq 255$. Figure 2.1 (a) shows the toy image with $f = 255$. Note that the origin of this data is the left bottom. The polynomial $G(u = \rho_u e^{i\phi_u}, v)$ of v for this image is the third order polynomial. The zero-values β_k's of $G(u = \rho_u e^{i\phi_u}, v)$ are $\beta_1 = -\rho_u^2 e^{2i\phi_u}$, $\beta_2 = \sqrt{\rho_u} e^{i(\phi_u+\pi)/2}$ and $\beta_3 = \sqrt{\rho_u} e^{i(\phi_u+3\pi)/2}$. Note that the β_k's do not contain f. When ϕ_u is varied form 0 to 2π for a fixed ρ_u, β_1 forms a circle alone, on the other hand β_2 and β_3 form a circle as a group. In this sense, β_1, β_2 and β_3 are classified into two groups $\{\beta_1\}$ and $\{\beta_2, \beta_3\}$. It is instructive to represent the three zero-values on complex plane. As seen in Fig. 2.1 (b), for $\rho_u = 1$ β_k's are all degenerated on a unit circle. On the other hand, for $\rho_u \neq 1$ they are split into two circles, as seen in Fig. 2.1 (c). In this simple example, such degeneration of β_k's for $\rho_u = 1$ causes no problem because β_k's are given analytically and the classification of β_k's into groups can be done with the analytical form of β_k's. In actual images, however, zero-values of $G(u = \rho_u e^{i\phi_u}, v)$ are obtained only numerically because the sizes of the images are large. In such actual images of large sizes, for $\rho_u = 1$ the zero-values are generally overcrowded to the neighborhood of a unit circle on complex plane. This situation makes the classification of zero-values difficult. Therefore, in the deconvolution of actual images we have to take as $\rho_u \neq 1$ to classify the zero-values into groups correctly. In the deconvolution of actual images it is

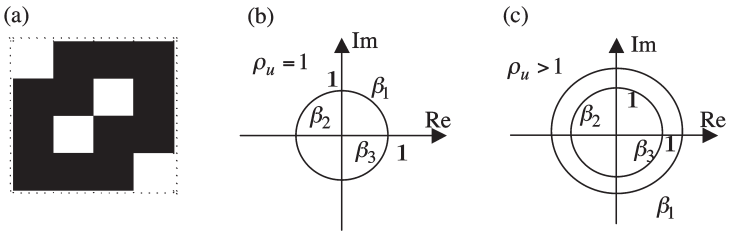

Fig. 2.1 (a) A toy model-image of the size 4 × 4, (b) The zero-sheet of the toy image for $\rho_u = 1$, (c) The zero-sheet of the toy image for $\rho_u > 1$.

very important how we choose an optimal value of ρ_u. In fact this is a very difficult problem because if we take ρ_u to be very different from unity we need multi-bytes computation in obtaining the zero-sheet. We will discuss this delicate point in detail in the next section.

Once we determine $F(u, v)$ in $u - v$ space by removing $H(u, v)$, we have to transform $F(u, v)$ to $f(x, y)$ to visualize the restored image. This is performed by the inverse Fourier transform. As we mentioned below Eq. (2.1), if we take u and v as $u = e^{-2\pi i\xi/M'}$ and $v = e^{-2\pi i\eta/N'}$, we have

$$F(\xi, \eta) = \frac{1}{M'N'} \sum_{x=0}^{M'-1} \sum_{y=0}^{N'-1} f(x, y)\rho_u^x \rho_v^y \exp\left(-2\pi i \frac{\xi x}{M'}\right)\exp\left(-2\pi i \frac{\eta y}{N'}\right). \tag{2.10}$$

This is just the two-dimensional discrete Fourier transform of $f(x, y)\rho_u^x \rho_v^y$. Therefore, the restored image in $x - y$ space is given, by the inverse Fourier transform, as

$$f(x, y)=\rho_u^{-x}\rho_v^{-y} \sum_{\xi=0}^{M'-1} \sum_{\eta=0}^{N'-1} F(\xi, \eta)\exp\left(2\pi i \frac{\xi x}{M'}\right)\exp\left(2\pi i \frac{\eta y}{N'}\right). \tag{2.11}$$

Note that the size of the restored image is taken as $M' \times N'$, which is the same as that of the observed image. As seen in Eq. (2.2) the size of the restored image $f(x, y)$ must be smaller than that of the observed image. However, in our analysis in the following sections, we reconstruct restored images in the same matrix space as that of the observed image.

3. A test of the Bates' blind deconvolution with a model image

In Sec. 2 we have given an overview of the basic idea of the Bates' blind deconvolution. Before we apply the Bates' blind deconvolution to the restoration of PET images we tested it with a model image. In this section, we present the result of the test. This is also a demonstration of the Bates' method. Figures 3.1 (a) and 3.1 (b) show an original image and a blur-image, respectively. Their sizes are 32×32 and 4×4, respectively. Note that the blur-image is the same one as the toy-image that we have used in explaining the basic structure of zero-sheets. Figure 3.2 shows the deteriorated image that was obtained by the convolution of the original and blur images. With this deteriorated image we tested the algorithm of the Bates' blind deconvolution. As we explained in Sec. 2, in order to classify zero-values we have to choose an optimal value of the parameter ρ (in this test we take as $\rho_u = \rho_v = \rho$). Figure 3.3 exhibits zero-sheets of v for various values of ρ. As seen in the figure, for $\rho = 1$ zero-values β_k's are overcrowded to the surroundings of a unit circle. We mentioned this situation in Sec. 2. In order to classify β_k's well, it seems better to take ρ to be different from unity as much as possible. However, this causes another problem due to the factor ρ^{x+y} in the polynomial of Eq. (2.6). The sizes of actual images are at least an order of 100×100. For such image sizes, the maximal power of ρ is of the order of 198. For $\rho = 1.5$, this gives $1.5^{198} \approx 10^{35}$. This causes loss of information of the image. We will discuss this severe problem in the image processing again in the next section. In the pres-

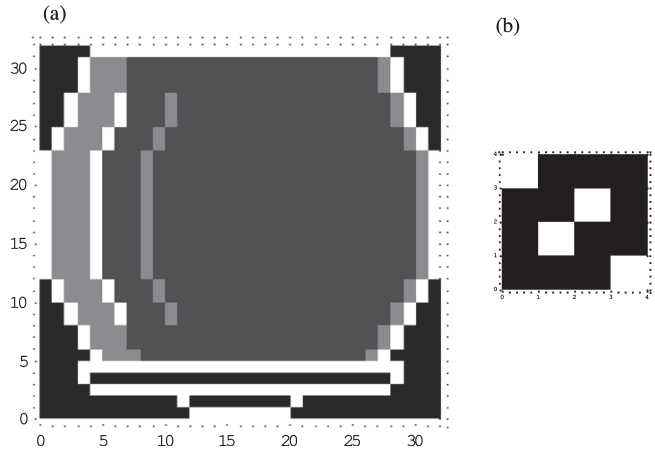

Fig. 3.1 (a) A model image (pot) of the size 32 × 32. (b) A blur-image of the size 4 × 4.

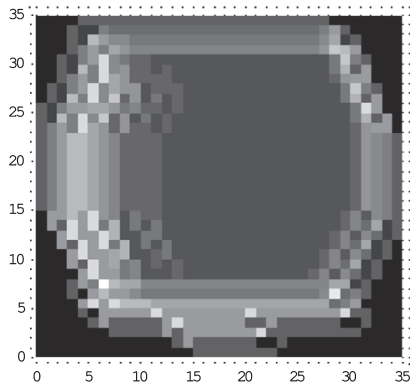

Fig. 3.2 The deteriorated image by convolution of the bur-image of Fig. 3.1 (b). The size of the image is 35 × 35.

ent analysis we calculate with the precision of forty digits, to save the processing time. Therefore, $\rho = 1.3$ or $\rho = 0.7$ is nearly the limit for no loss of information of the image. In this test we adopt $\rho = 1.3$ eventually.

In Fig. 3.4 we show the fine structure of the zero-sheet of v for $\rho = 1.3$. The size of the model image is 35 × 35 (note $M' + m - 1 = 32 + 4 - 1 = 35$). The number of zero-values β_k's of the polynomial $G(u = \rho_u e^{i\phi_u}, v)$ is 34 including degenerate zero-values. In Fig. 3.4 we plotted β_k's for every $\Delta\phi = 2\pi/986$. The total number of points plotted on the complex plane is 33524. In order to classify β_k's into groups we have to connect each β_k from $\phi = 0$ to 2π correctly. In the present case, it is not so difficult to connect each β_k. As the model image shown in Fig. 3.3 is small and simple enough, the zero-sheet is very simple. If we take $\Delta\phi$ small enough we can connect each β_k easily and classify β_k's into some groups correctly. For actual images, however, this is an extremely tough work. To make it possible to connect each β_k of any complicated zero-sheets of actual images, we developed a technical

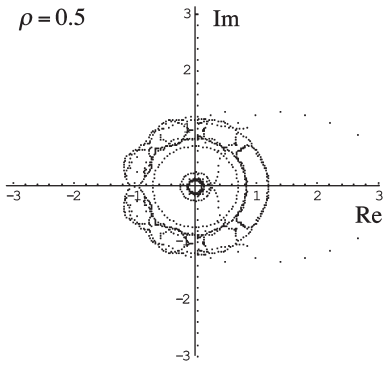
ρ = 0.5
Im
Re

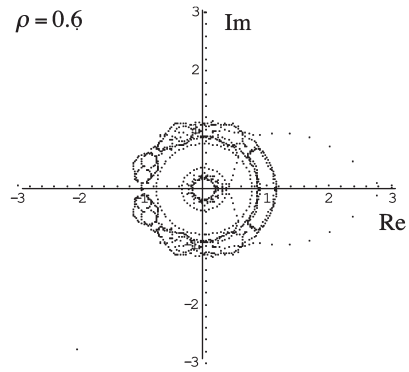
ρ = 0.6
Im
Re

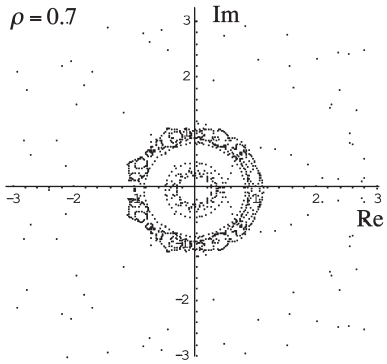
ρ = 0.7
Im
Re

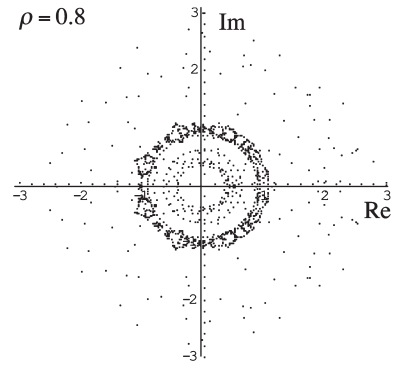
ρ = 0.8
Im
Re

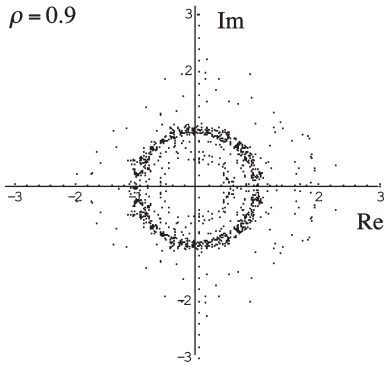
ρ = 0.9
Im
Re

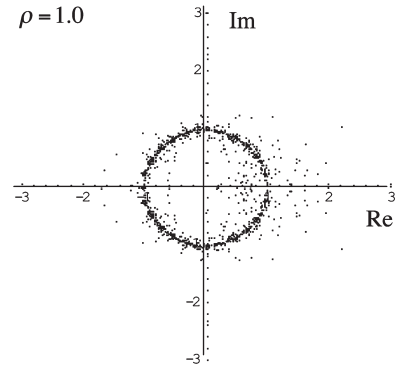
ρ = 1.0
Im
Re

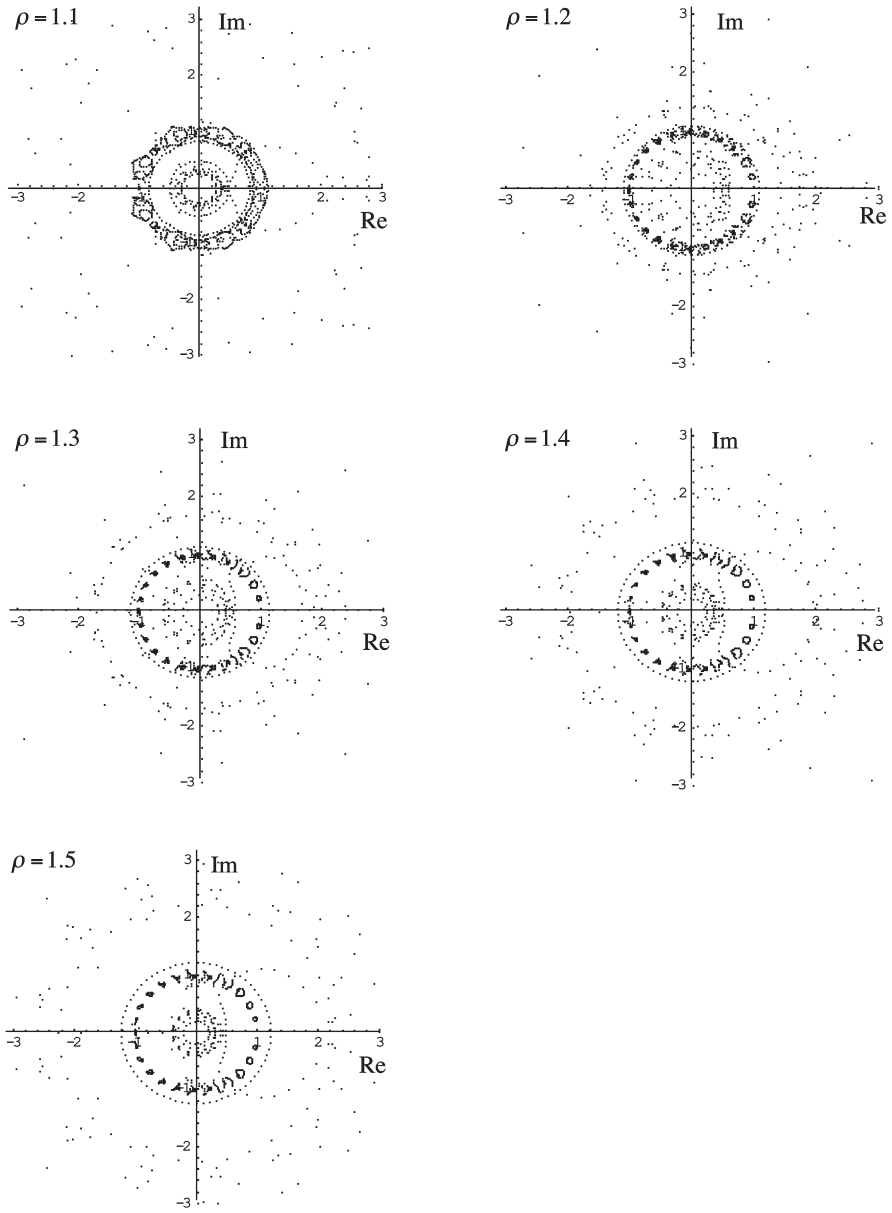

Fig. 3.3 The zero-sheets of v of the model image of Fig. 3.2.

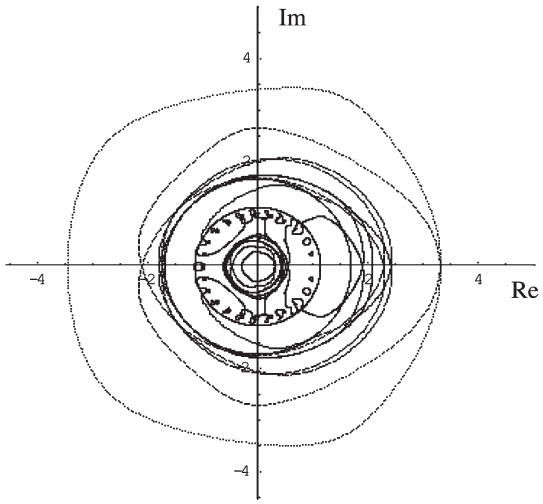

Fig. 3.4 The fine structure of the zero-sheet of v for $\rho = 1.3$.

method. We discuss this in detail in Sec. 4. In the present demonstration we connected each β_k from $\phi = 0$ to 2π by taking $\Delta\phi$ small enough. Figure 3.5 shows the connected β_k's. The 34 β_k's are connected correctly. As seen at a glance, β_1, β_{17} and β_{18} belong to those of the blur-image of the size 4 × 4 (see Fig. 2.1). Figure 3.5 exhibits the zero-sheet where zero-sheets of the blur-image β_1, β_{17} and β_{18} have been removed.

As we have explained in Sec. 2, in order to reconstruct the original image we have to repeat the same processing for u. Figure 3.7 (a) shows the zero-sheet of u, which consists of 34 zero-values γ_k's of u. The zero-sheet of u for the blur-image should be the same as that of v because the blur-image of this case is symmetric for x and y. Figure 3.7 (b) shows the zero-sheet of u, where the zero-sheet of the blur-image has been removed.

Now we can reconstruct an image from the zero-sheets shown in Figs. 3.6 and 3.7 (b). Figure 3.8 (a) shows $F(\xi, \eta)$ of the image reconstructed from the zero-sheet of v shown in Fig. 3.6. Figure 3.8 (b) shows $F(\xi, \eta)$ of the image reconstructed from the zero-sheet of u shown in Fig. 3.7 (b). Figure 3.9 exhibits $F(\xi, \eta)$ that was obtained by readjusting the two $F(\xi, \eta)$'s shown in Figs. 3.8 (a) and 3.8 (b). A restored image in $x - y$ space is obtained by the inverse Fourier transform of $F(\xi, \eta)$ shown in Fig. 3.9. Figure 3.10 (a) shows $f(x, y)\rho^{x+y}$ obtained from $F(\xi, \eta)$ of Fig. 3.9 by the inverse Fourier transform. Figure 3.10 (b) is the restored image $f(x, y)$. As seen in the figure, the restored image is the same as the original-image (pot) of Fig. 3.1 (a). Note that the restored image of the size 32 × 32 is embedded in 35 × 35 matrix space that is the space of the deteriorated image of Fig. 3.2. The demonstration presented in this section shows that the Bates' zero-sheet method seems to work well for this kind of simple and small image.

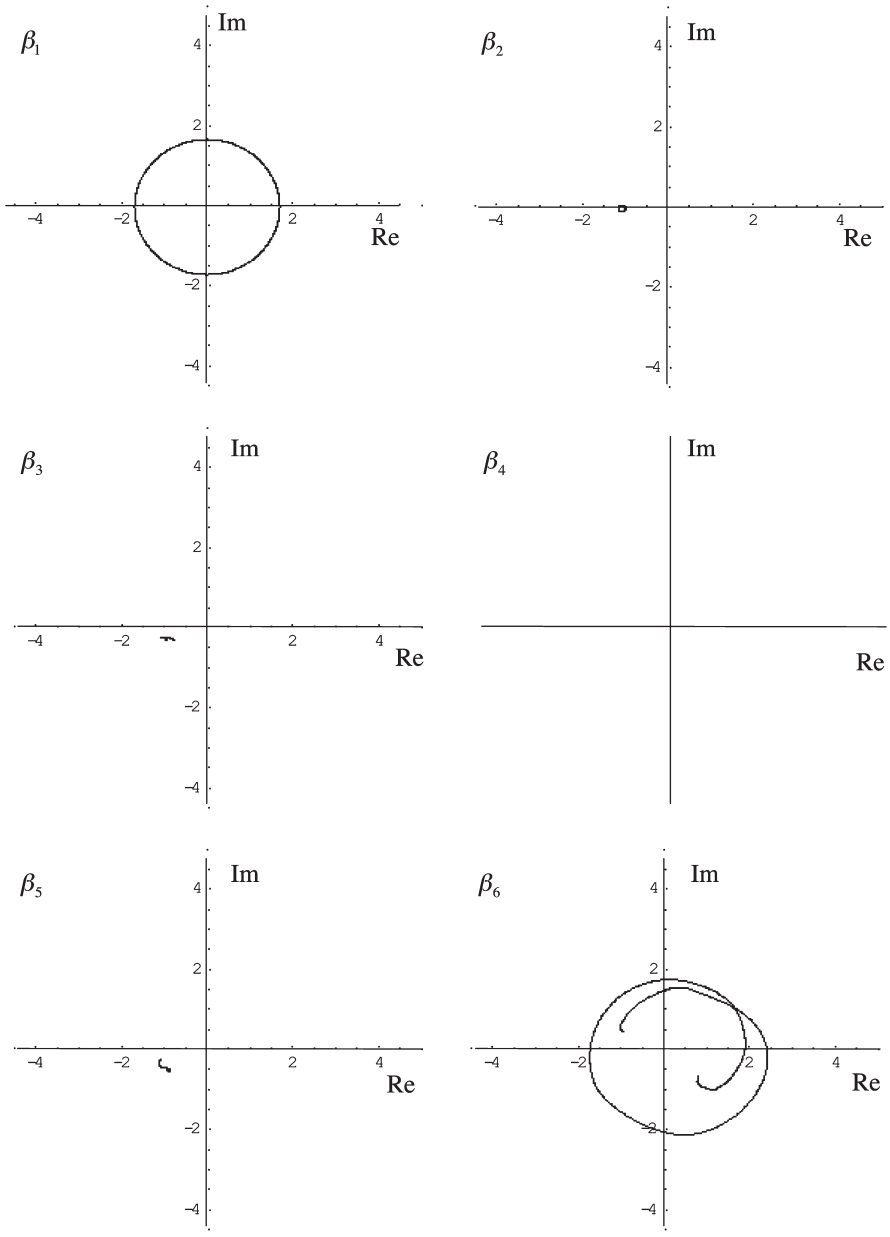
β_1
Im
Re
β_2
Im
Re
β_3
Im
Re
β_4
Im
Re
β_5
Im
Re
β_6
Im
Re

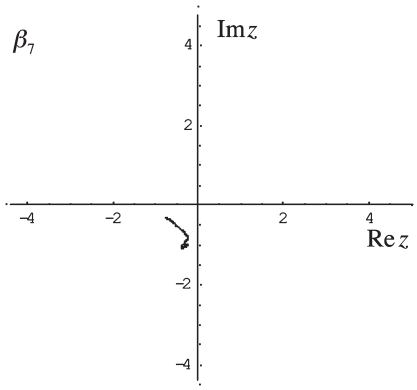
β_7
Im z
Re z
4
2
−4
−2
2
4
−2
−4

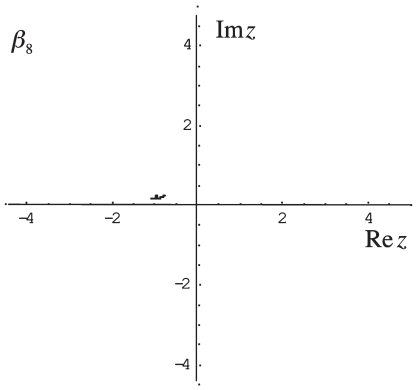
β_8
Im z
Re z
4
2
−4
−2
2
4
−2
−4

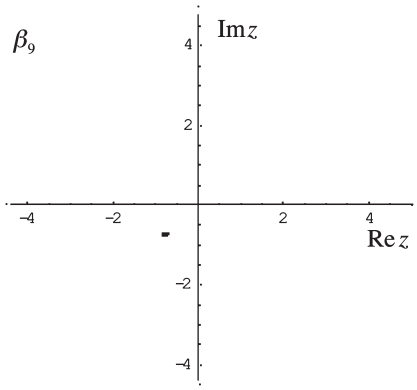
β_9
Im z
Re z
4
2
−4
−2
2
4
−2
−4

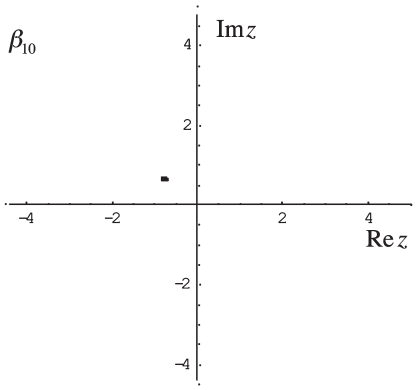
β_{10}
Im z
Re z
4
2
−4
−2
2
4
−2
−4

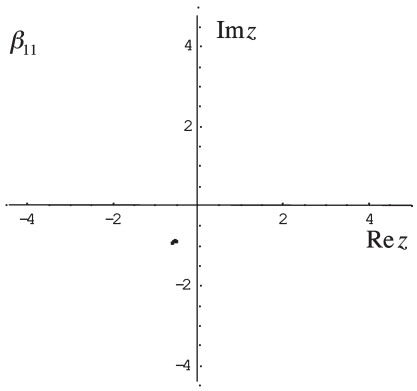
β_{11}
Im z
Re z
4
2
−4
−2
2
4
−2
−4

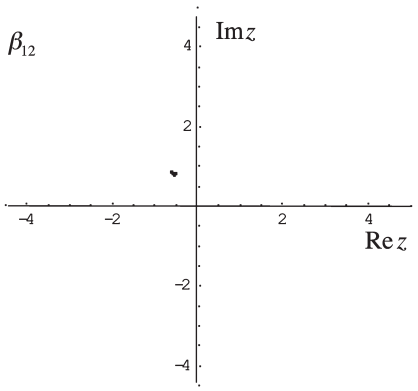
β_{12}
Im z
Re z
4
2
−4
−2
2
4
−2
−4

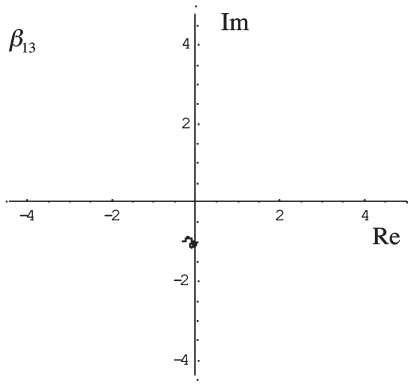
β_{13}
Im
Re
4
2
−4
−2
2
4
−2
−4

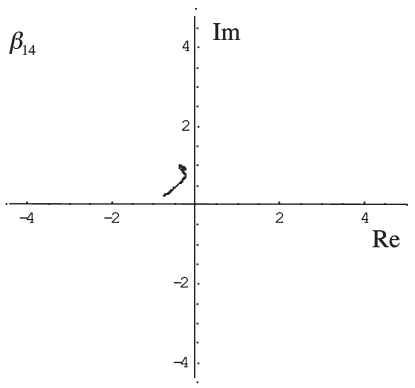
β_{14}
Im
Re
4
2
−4
−2
2
4
−2
−4

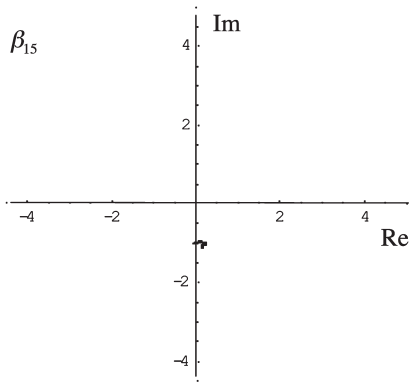
β_{15}
Im
Re
4
2
−4
−2
2
4
−2
−4

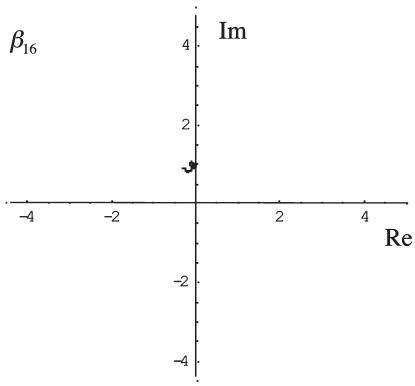
β_{16}
Im
Re
4
2
−4
−2
2
4
−2
−4

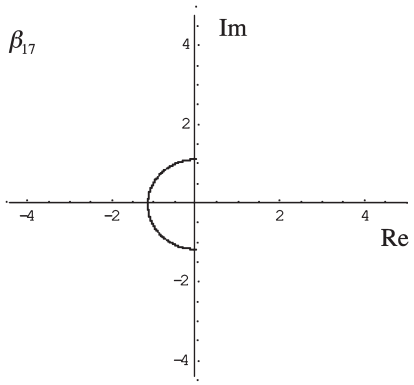
β_{17}
Im
Re
4
2
−4
−2
2
4
−2
−4

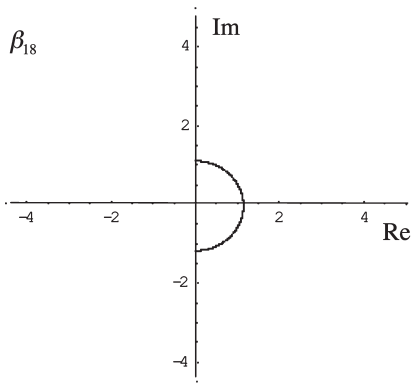
β_{18}
Im
Re
4
2
−4
−2
2
4
−2
−4

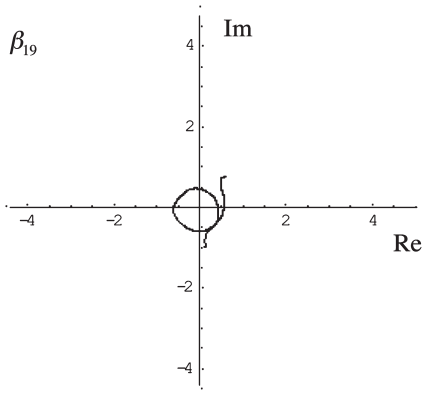
β_{19}
Im
Re
4
2
−4
−2
2
4
−2
−4

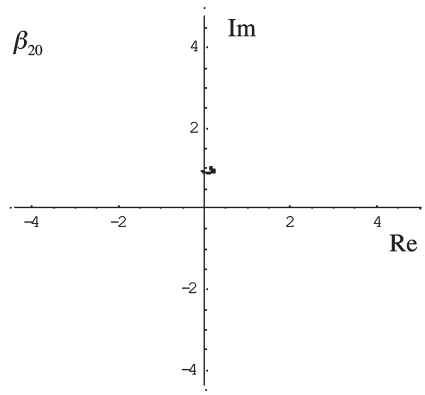
β_{20}
Im
Re
4
2
−4
−2
2
4
−2
−4

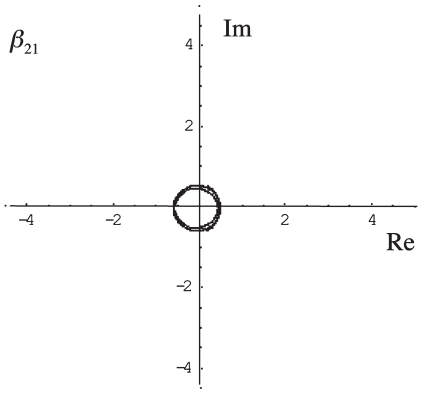
β_{21}
Im
Re
4
2
−4
−2
2
4
−2
−4

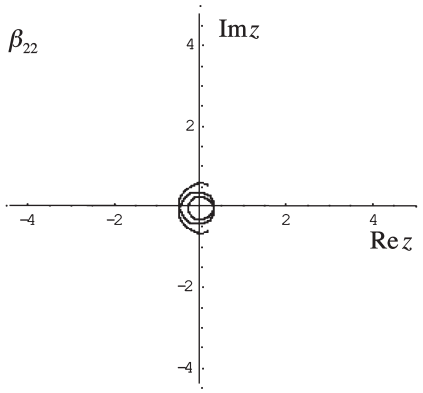
β_{22}
Imz
Rez
4
2
−4
−2
2
4
−2
−4

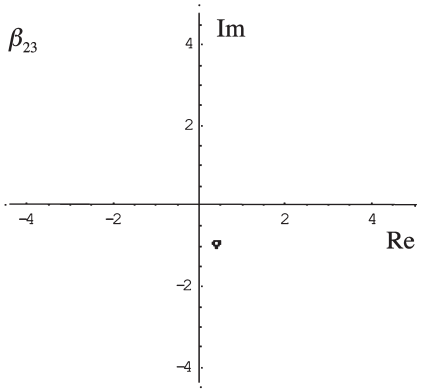
β_{23}
Im
Re
4
2
−4
−2
2
4
−2
−4

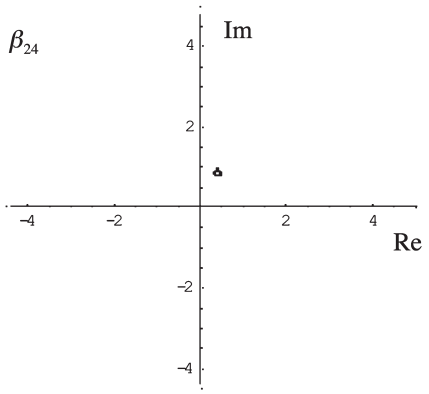
β_{24}
Im
Re
4
2
−4
−2
2
4
−2
−4

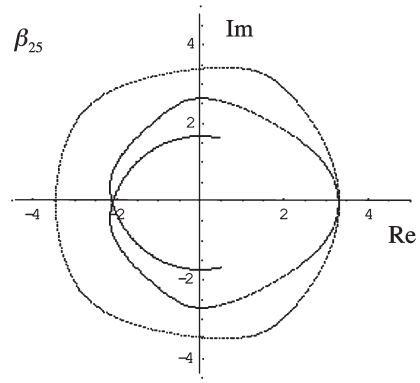
β_{25}
Im
Re

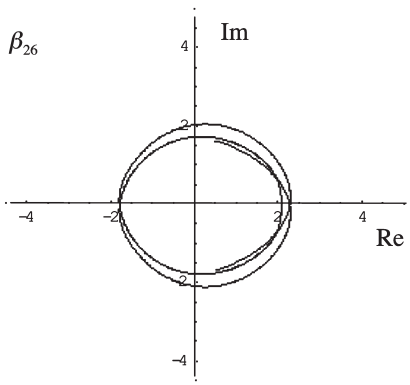
β_{26}
Im
Re

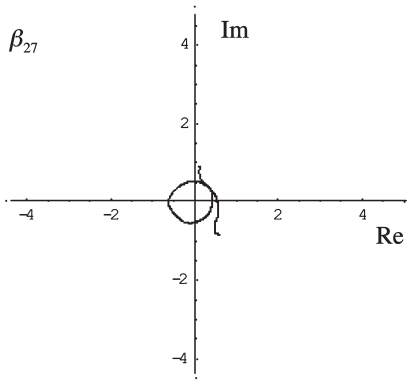
β_{27}
Im
Re

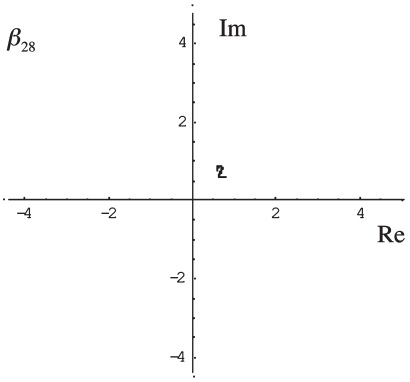
β_{28}
Im
Re

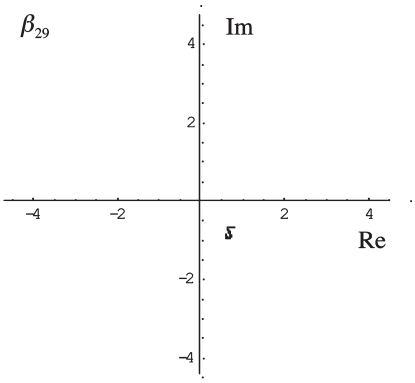
β_{29}
Im
Re

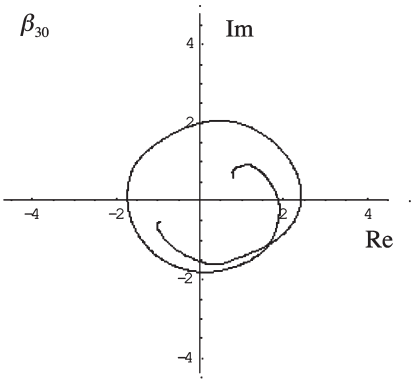
β_{30}
Im
Re

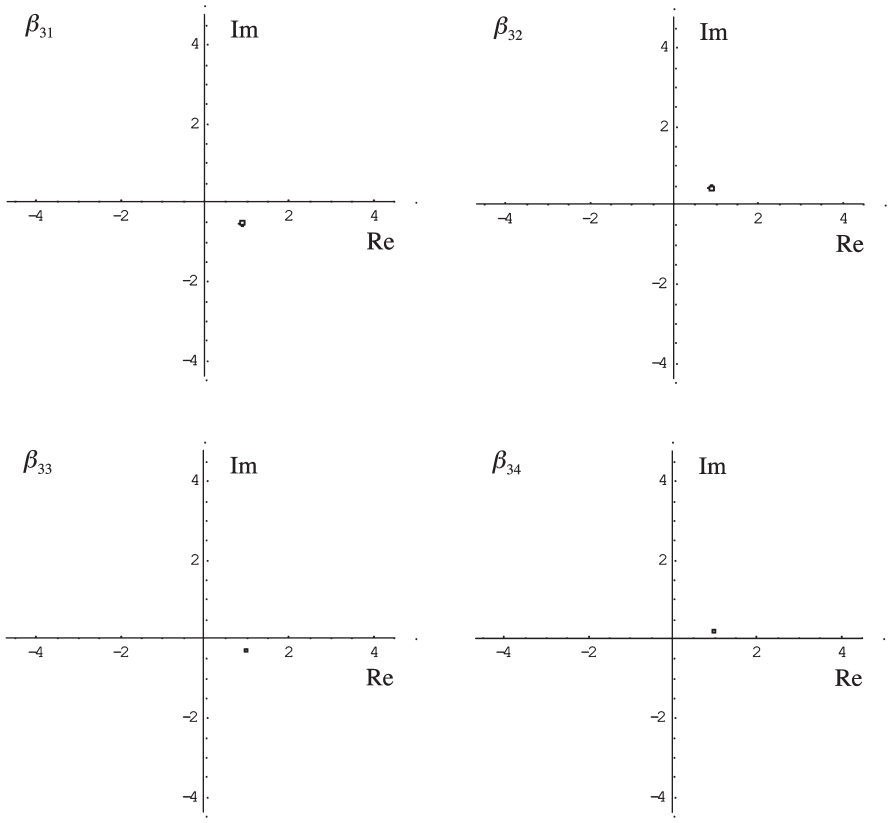

Fig. 3.5 Connected zero-values β_k's of v.

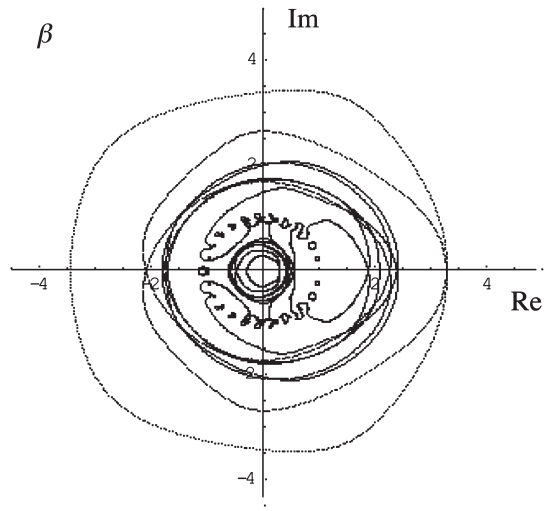

Fig. 3.6 The zero-sheet of v, where the zero-sheets of the blur-image β_1, β_{17} and β_{18} were removed.

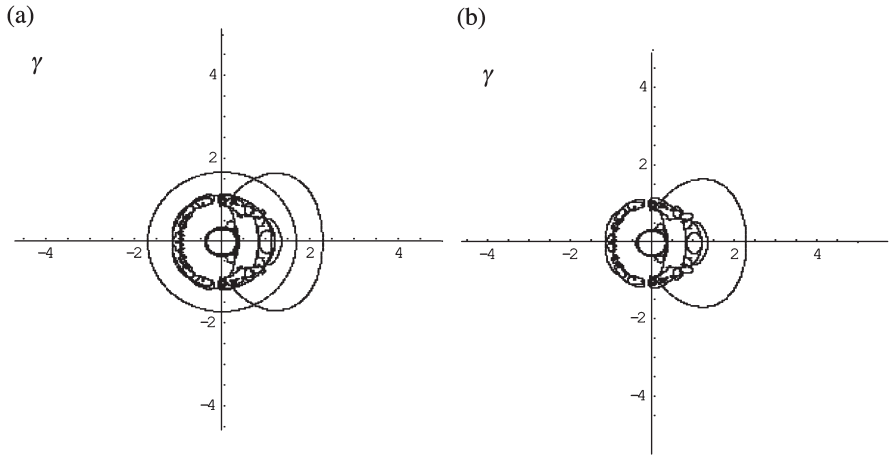

Fig. 3.7 (a) The zero-sheet of u. (b) The zero-sheet of u where the zero-sheet of the blur was removed.

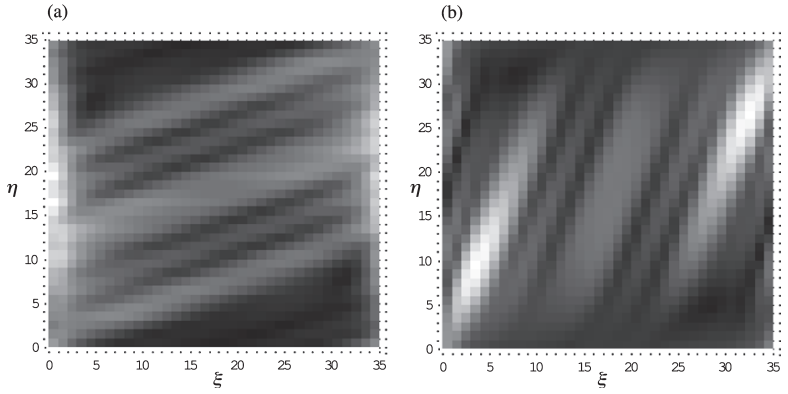

Fig. 3.8 (a) $F(\xi, \eta)$ of the image that was reconstructed from the zero-sheet of v shown in Fig3.6. (b) $F(\xi, \eta)$ of the image that was reconstructed from the zero-sheet of u shown in Fig. 3.7 (b).

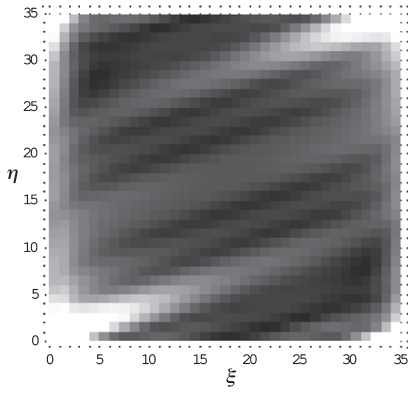

Fig. 3.9 $F(\xi, \eta)$ obtained by readjusting $F(\xi, \eta)$'s of Figs. 3.8 (a) and 3.8 (b).

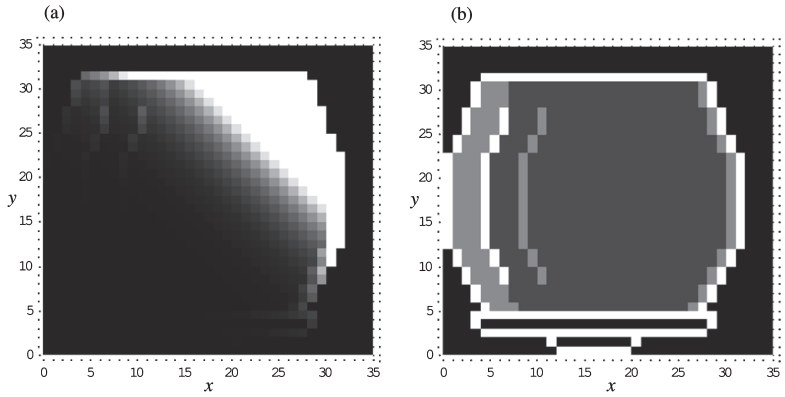

Fig. 3.10 (a) $f(x, y)\rho^{x+y}$ obtained from $F(\xi, \eta)$ of Fig. 3.9. (b) The restored image $f(x, y)$.

4. Technical tools for the Bates' zero-sheet method

4.1 Connection method of zero-values by a differential equation

In the preceding section, we demonstrated the image processing by the Bates' Zero-sheet method and showed that it works very well for a simple and small image. Our purpose is to apply the zero-sheet method to restoring actual PET images. As mentioned in the preceding section, we obtain zero-values $\beta_k(\gamma_k)$ by solving $G(u = \rho_u e^{i\phi_u}, v) = 0$ ($G(u, v = \rho_v e^{i\phi_v}) = 0$) for every $\Delta\phi_u$ ($\Delta\phi_v$) in a desired accuracy. In order to judge zero-sheets of blur-images, first we have to connect each $\beta_k(\gamma_k)$ from $\Delta\phi_u$ ($\Delta\phi_v$) = 0 to 2π correctly. In the demonstration that we presented in Sec. 3 the sample image was simple and small enough, and the zero-sheet of the sample image was very simple. Accordingly, we could connect the zero-values by taking $\Delta\phi$ small enough. However, as we illustrate in the following, for actual PET images it is extremely difficult to connect each zero-values from $\phi = 0$ to 2π because their zero-sheets are very complicated.

Fig. 4.1.1 shows a PET image that we downloaded from the web site http://www.rad.kumc.edu/nucmed/clinical/pet_lung2.htm. It represents a PET image of a cross section of a human body. Note that in Fig. 4.1.1 we reversed the brightness. Figure 4.1.2 shows the zero-sheet of v for the PET image, where 67 β_k's calculated with $\rho_u = 1.1$ are plotted for every $\Delta\phi_u = 2\pi/670$. Since ρ_u is very close to unity, the zero-values are overcrowded in the neighborhood of a unit circle. We mentioned this situation in Sec. 3. Further, although the PET image of Fig. 4.1.1 looks rather simple compared to the model image (pot) of Fig. 3.2, the zero-sheet for the PET image is more complicated than that of the model image (see Fig. 3.4).

As we have just illustrated above, in actual images their zero-sheets have very complicated structures in general. Therefore, we need a technical tool to connect each $\beta_k(\gamma_k)$ calculated for every $\Delta\phi_u(\Delta\phi_v)$. In the present work, we developed a method for connecting each $\beta_k(\gamma_k)$ by a differential equation. The algorithm of the method is illustrated in Fig. 4.1.3. The zero-values $\beta_k(\gamma_k)$ of the polynomials $G(u = \rho_u e^{i\phi_u}, v)$ ($G = (u, v = \rho_v e^{i\phi_v})$) are calculated in a desired accuracy, which must be enough accuracy not to lose information of given

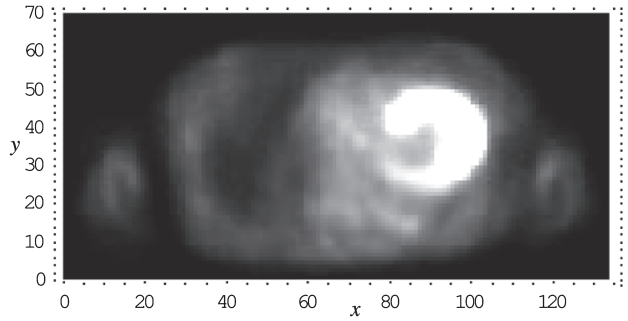

Fig. 4.1.1 A PET image of cross section of a human body that was downloaded from the web site http://www.rad.kumc.edu/nucmed/clinical/pet_lung2.htm. Note that we reversed the brightness.

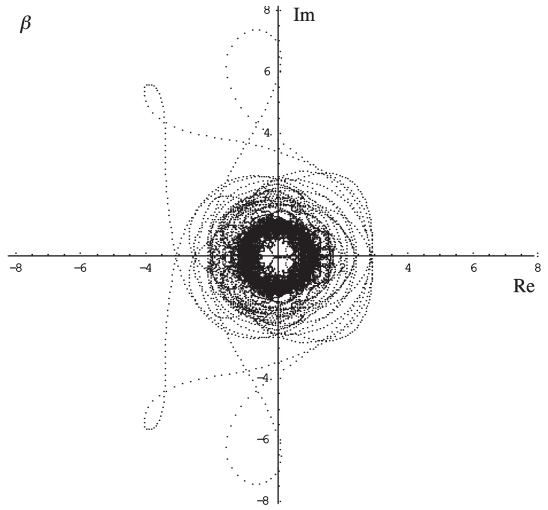

Fig. 4.1.2 The zero-sheet of variable υ for the PET image of Fig. 4.1.1, where ρ_u is taken as 1.1.

images. In this work we use *Mathematica* to calculate β_k's (γ_k's) in a desired accuracy. Small circles in Fig. 4.1.3 represent the β_k's (γ_k's) of $G(u = \rho_u e^{i\phi_u}, \upsilon)$ ($G(u, \upsilon = \rho_\upsilon e^{i\phi_\upsilon})$) calculated for every $\Delta\phi_u(\Delta\phi_\upsilon)$. In this method, we do not have to take $\Delta\phi_u(\Delta\phi_\upsilon)$ very small to connect each $\beta_k(\gamma_k)$. However, we have to take $\Delta\phi_u(\Delta\phi_\upsilon)$ at least to be $2\pi/M'$ ($2\pi/N'$) because we need $F(u = \rho_u e^{i\phi_u}, \upsilon)$ and $F(u, \upsilon = \rho_\upsilon e^{i\phi_\upsilon})$ at those points for the inverse Fourier transform. Once we obtain β_k's (γ_k's) in a desired accuracy for every $\Delta\phi_u(\Delta\phi_\upsilon)$, we connect $\beta_k(\rho_u, l\Delta\phi_u)$ and $\beta_k(\rho_u, (l + 1)\Delta\phi_u)$ ($l = 0,1,\ldots, M' - 1$) ($\gamma_k(\rho_\upsilon, l\Delta\phi_\upsilon)$ and $\gamma_k(\rho_\upsilon, (l + 1)\Delta\phi)$ ($l = 0, 1, \ldots, N' - 1$)) by solving a differential equation. Computational errors in solving the differential equation are reset if $\beta_k(\rho_u, l\Delta\phi_u)$ and $\beta_k(\rho_u, (l + 1)\Delta\phi_u)$ ($(\gamma_k(\rho_\upsilon, l\Delta\phi_\upsilon)$ and $\gamma_k(\rho_\upsilon, (l + 1)\Delta\phi)$) are connected correctly.

The differential equation for $\beta_k(\rho_u, \phi_u)$ ($k = 1, 2, \ldots, N'$) with respect to ϕ_u at a given $\rho_u = \rho_0$ is written as

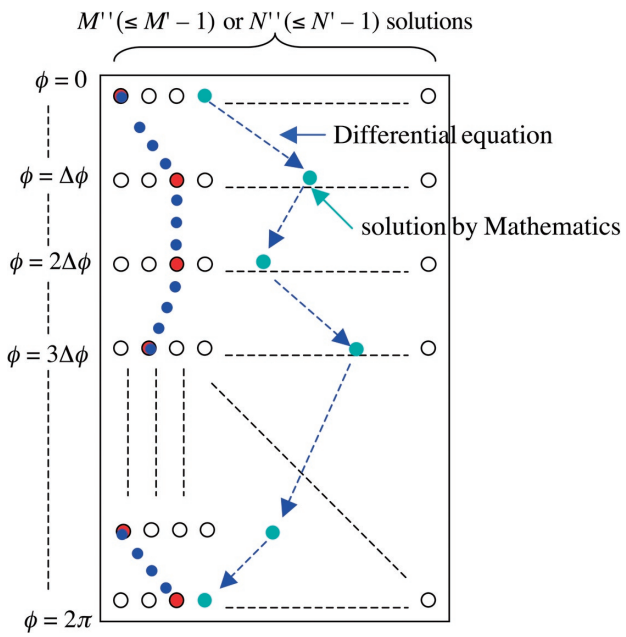

Fig. 4.1.3 The algorithm to connect each $\beta_k(\gamma_k)$. The ϕ means ϕ_u or ϕ_v.

$$\left.\frac{d\beta_k(\rho_u=\rho_0,\phi_u)}{d\phi_u}\right|_{\rho_u=\rho_0} = -\left.\frac{\left(\frac{\partial G}{\partial \phi_u}\right)}{\left(\frac{\partial G}{\partial \beta_k}\right)}\right|_{\rho_u=\rho_0}, \tag{4.1.1}$$

where

$$\frac{\partial G}{\partial \phi_u} = \frac{1}{M'N'}\sum_{x=0}^{M'-1}\sum_{y=0}^{N'-1} g(x,y)ix(\rho_u e^{i\phi_u})^x {\beta_k}^y \tag{4.1.2}$$

and

$$\frac{\partial G}{\partial \beta_k} = \frac{1}{M'N'}\sum_{x=0}^{M'-1}\sum_{y=0}^{N'-1} g(x,y)(\rho_u e^{i\phi_u})^x y{\beta_k}^{y-1}. \tag{4.1.3}$$

The differential equation (4.1.1) is actually simultaneous equations of its real and imaginary parts. The differential equation for $\gamma_k(\rho_v, \phi_v)$ (k = 1, 2, …, M'') is obtained by $\beta_k \to \gamma_k$, $\rho_u \to \rho_v$, $\phi_u \to \phi_v$ and $x \leftrightarrow y$ in Eqs. (4.1.1)–(4.1.3), but $g(x, y)$ must be left as just as it is. The differential equation is powerful. To test the power we tried to connect each β_k shown in Fig. 4.1.2. Figure 4.1.4 is the result. As seen in the figure, 67 β_k's are well classified into four closed curves. Thus, the connection method by the differential equation (4.1.1) works very well even for the overcrowded zero-sheet such as that shown in Fig. 4.1.2.

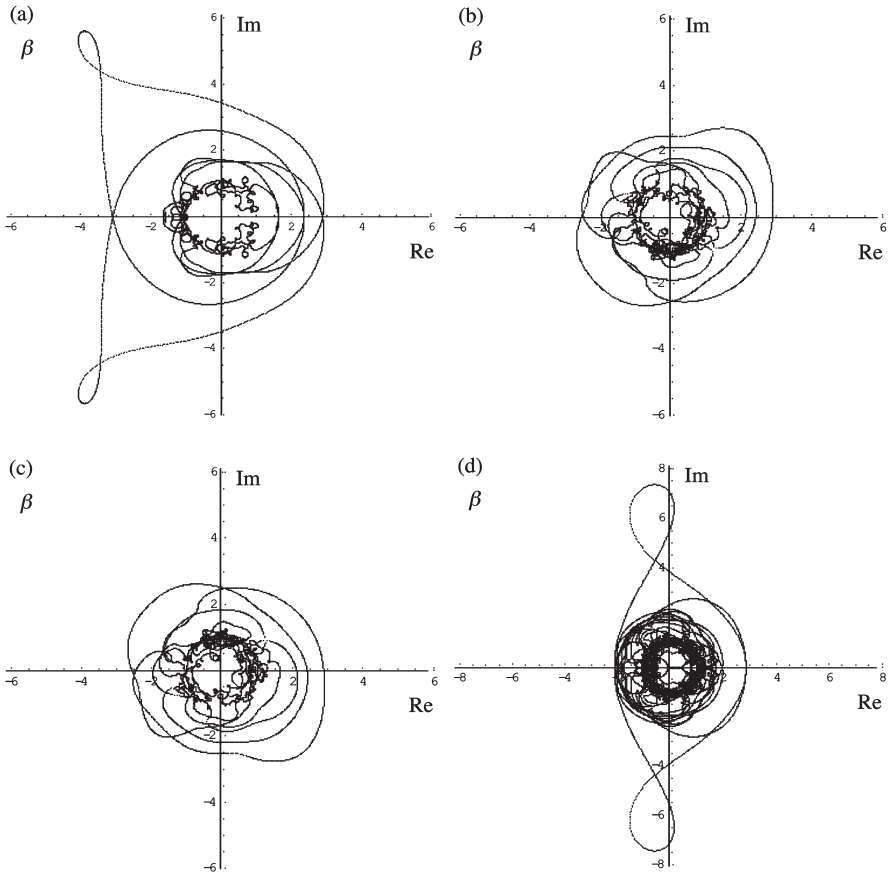

Fig. 4.1.4 The zero-values β_k's that were classified by the differential equation (4.1.1).

4.2 Conditional expression for judging a blur element of a small size

In the preceding section we have presented a powerful tool for connecting any zero-values that compose complicated zero-sheets. By connecting zero-values with the tool we can classify the zero-values into groups. By examining the classified zero-values we can judge which zero-values are those of blurs. On the other hand, if it is possible to judge any blurs without connecting and classifying zero-values, it is very significant for the Bates' blind deconvolution. We examined this problem and found that in principle it is possible to derive a conditional expression by which we can judge a blur without classifying the zero-values. The conditional expression we found is for blur-images of the size 2 × 2. For each β_k ($k = 0, 1, \ldots, N' - 1$) of $G(u = \rho_u e^{i\phi_u}, v)$ the conditional expression is expressed as

$$\left(\frac{d\beta_k(\rho_u,\ \phi_u = \phi_i)}{d\rho_u}\right)\left(\frac{d^3\beta_k(\rho_u,\ \phi_u = \phi_i)}{d{\rho_u}^3}\right) = \frac{3}{2}\left(\frac{d^2\beta_k(\rho_u,\ \phi_u = \phi_i)}{d{\rho_u}^2}\right)^2, \tag{4.2.1}$$

where the derivatives of β_k with respect to ρ_u are given analytically as

$$\frac{d\beta_k(\rho_u,\ \phi_u=\phi_i)}{d\rho_u}=-\left.\frac{\left(\dfrac{\partial G}{\partial \rho_u}\right)}{\left(\dfrac{\partial G}{\partial \beta_k}\right)}\right|_{\phi_u=\phi_i}, \tag{4.2.2}$$

$$\frac{d^2\beta_k(\rho_u,\ \phi_u=\phi_i)}{d{\rho_u}^2}=-\frac{1}{\left(\dfrac{\partial G}{\partial \beta_k}\right)}\left.\left\{\frac{\partial^2 G}{\partial {\rho_u}^2}+2\frac{\partial^2 G}{\partial \rho_u \partial \beta_k}\left(\frac{d\beta_k}{d\rho_u}\right)+\frac{\partial^2 G}{\partial {\beta_k}^2}\left(\frac{d\beta_k}{d\rho_u}\right)^2\right\}\right|_{\phi=\phi_i}, \tag{4.2.3}$$

$$\begin{aligned}\frac{d^3\beta_k(\rho_u,\ \phi_u=\phi_i)}{d{\rho_u}^3}=&-\frac{1}{\left(\dfrac{\partial G}{\partial \beta_k}\right)}\left\{\frac{\partial^3 G}{\partial {\rho_u}^3}+3\frac{\partial^3 G}{\partial {\rho_u}^2\partial \beta_k}\left(\frac{d\beta_k}{d\rho_u}\right)+3\frac{\partial^3 G}{\partial \rho_u \partial {\beta_k}^2}\left(\frac{d\beta_k}{d\rho_u}\right)^2\right.\\&\left.+3\frac{\partial^2 G}{\partial \rho_u \partial \beta_k}\left(\frac{d^2\beta_k}{d{\rho_u}^2}\right)+3\frac{\partial^2 G}{\partial {\beta_k}^2}\left(\frac{d\beta_k}{d\rho_u}\right)\left(\frac{d^2\beta_k}{d{\rho_u}^2}\right)+\frac{\partial^3 G}{\partial {\beta_k}^3}\left(\frac{d\beta_k}{d\rho_u}\right)^3\right\}\Bigg|_{\phi_u=\phi_i},\end{aligned} \tag{4.2.4}$$

with

$$\frac{\partial G}{\partial \rho_u}=\frac{1}{M'N'}\sum_{x=0}^{M'-1}\sum_{y=0}^{N'-1} g(x,y)x{\rho_u}^{x-1}(e^{i\phi_u})^x{\beta_k}^y, \tag{4.2.5}$$

$$\frac{\partial G}{\partial \beta_k}=\frac{1}{M'N'}\sum_{x=0}^{M'-1}\sum_{y=0}^{N'-1} g(x,y)(\rho_u e^{i\phi_u})^x y{\beta_k}^{y-1}, \tag{4.2.6}$$

$$\frac{\partial^2 G}{\partial {\rho_u}^2}=\frac{1}{M'N'}\sum_{x=0}^{M'-1}\sum_{y=0}^{N'-1} g(x,y)x(x-1){\rho_u}^{x-2}(e^{i\phi_u})^x{\beta_k}^y, \tag{4.2.7}$$

$$\frac{\partial^2 G}{\partial \rho_u \partial \beta_k}=\frac{1}{M'N'}\sum_{x=0}^{M'-1}\sum_{y=0}^{N'-1} g(x,y)x{\rho_u}^{x-1}(e^{i\phi_u})^x y{\beta_k}^{y-1}, \tag{4.2.8}$$

$$\frac{\partial^2 G}{\partial {\beta_k}^2}=\frac{1}{M'N'}\sum_{x=0}^{M'-1}\sum_{y=0}^{N'-1} g(x,y)(\rho_u e^{i\phi_u})^x y(y-1){\beta_k}^{y-2}, \tag{4.2.9}$$

$$\frac{\partial^3 G}{\partial {\rho_u}^3}=\frac{1}{M'N'}\sum_{x=0}^{M'-1}\sum_{y=0}^{N'-1} g(x,y)x(x-1)(x-2){\rho_u}^{x-3}(e^{i\phi_u})^x{\beta_k}^y, \tag{4.2.10}$$

$$\frac{\partial^3 G}{\partial {\rho_k}^2 \partial \beta_k}=\frac{1}{M'N'}\sum_{x=0}^{M'-1}\sum_{y=0}^{N'-1} g(x,y)x(x-1){\rho_u}^{x-2}(e^{i\phi_u})^x y{\beta_k}^{y-1}, \tag{4.2.11}$$

$$\frac{\partial^3 G}{\partial \rho_u \partial {\beta_k}^2}=\frac{1}{M'N'}\sum_{x=0}^{M'-1}\sum_{y=0}^{N'-1} g(x,y)x{\rho_u}^{x-1}(e^{i\phi_u})^x y(y-1){\beta_k}^{y-2}, \tag{4.2.12}$$

$$\frac{\partial^2 G}{\partial \beta_k{}^2} = \frac{1}{M'N'} \sum_{x=0}^{M'-1} \sum_{y=0}^{N'-1} g(x, y)(\rho_u e^{i\phi_u})^x y(y-1)(y-2)\beta_k{}^{y-3}. \tag{4.2.13}$$

The conditional expression (4.2.1) is a relation among the first, second and third derivatives of $\beta_k(\rho_u, \phi_u)(k = 1, \ldots, N' - 1)$ with respect to ρ_u. The expression is very elegant in the sense that everything needed in evaluating the expression is given analytically. In order to judge whether or not a β_k is a zero-value of a blur-image of the size 2 × 2, we only substitute the numerical value of β_k into the conditional expression (4.2.1). Further, we can evaluate the expression for any ρ_u and ϕ_u. The conditional expression for $\gamma_k(\rho_v, \phi_v)(k = 1, \ldots, M' - 1)$ is obtained by $\beta_k \to \gamma_k$, $\rho_u \to \rho_v$, $\phi_u \to \phi_v$ and $x \leftrightarrow y$ in Eqs. (4.2.1)–(4.2.13), but $g(x, y)$ must be left as just as it is.

We test the utility of the conditional expression (4.2.1) using a test image shown in Fig. 4.2.1. The image is similar to that of Fig. 3.2 that we used in demonstrating the Bates' blind deconvolution. In the image of Fig. 3.2 a blur-image of the size 4 × 4 was convoluted. On the other hand, in the image of Fig. 4.2.1 a blur image of the size 2 × 2 is convoluted. The zero-sheets of v and u for the image of Fig. 4.2.1 are shown in Fig. 4.2.2. We test how the conditional expression (4.1.1) works well for the zero-values shown in Fig. 4.2.2. As we mentioned above, the expression (4.1.1) can be evaluated for any ρ_u and ϕ_u. In the present test we evaluate it for $\rho_u = 1.3$ and $\phi_u = 0$. Figure 4.2.3 (a) shows the result of the evaluation. As seen in the figure, β_5 satisfies the conditional expression of Eq. (4.2.1). Figure 4.2.3 (b) shows the zero-sheet of β_5. The zero-sheet shows a typical shape of a blur-image of the size 2 × 2. Similarly, Fig. 4.2.4 (a) shows the result of the evaluation of the conditional expression for γ_k. In this case, γ_1 satisfies the conditional expression for γ_k. Figure 4.2.4 (b) is the zero-sheet of γ_1.

In this way, we can judge that β_5 and γ_1 are the zero-values of v and u of a blur-image of the size 2 × 2. In Fig. 4.2.5 we show the zero-sheets where the zero-sheets of the blur-image have been removed.

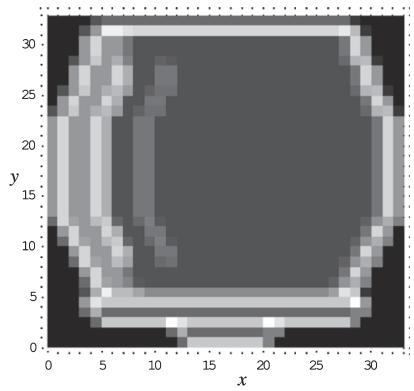

Fig. 4.2.1 A test image that was deteriorated by convolution of a blur-image of the size 2 × 2. The size of the image is 33 × 33.

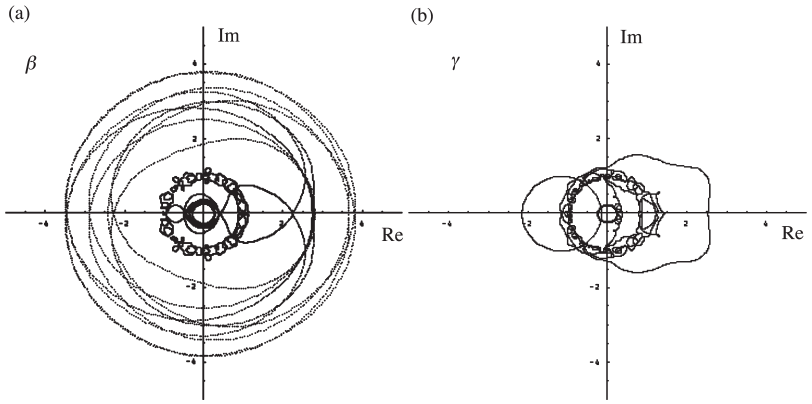

Fig. 4.2.2 (a) The zero-sheet of v for the image shown in Fig. 4.2.1. (b) The zero-sheet of u for the image shown in Fig. 4.2.1. The parameters ρ_u and ρ_v are taken as $\rho_u = \rho_v = 1.3$.

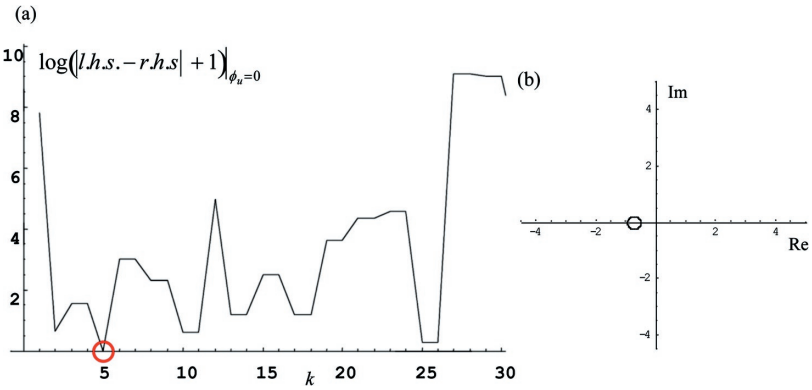

Fig. 4.2.3 (a) Evaluation of the conditional expression (4.2.1) by β_k, k = 1, …, 33. (b) The zero-sheet of β_5, where ρ_u is taken as 1.3.

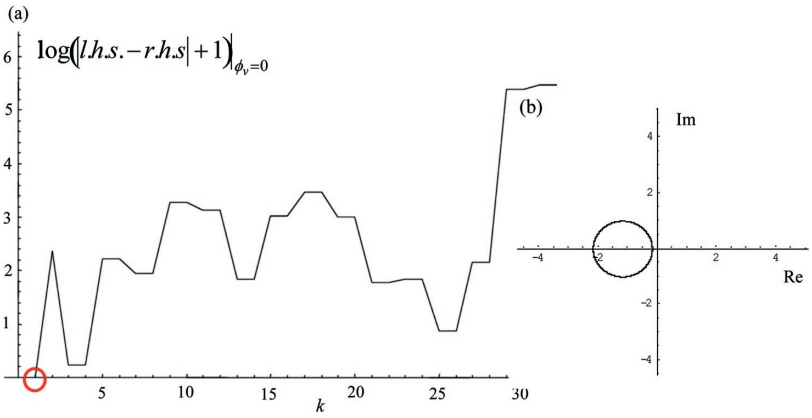

Fig. 4.2.4 (a) Evaluation of the conditional expression for γ_k, k = 1, …, 33. (b) The zero-sheet of γ_1, ρ_v is taken as 1.3.

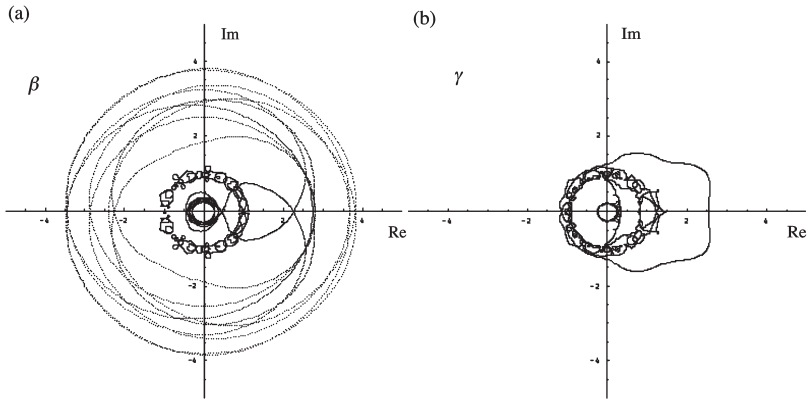

Fig. 4.2.5 (a) The zero-sheet of v, where the zero-sheet of β_5 was removed. (b) The zero-sheet of u, where the zero-sheet of γ_1 was removed.

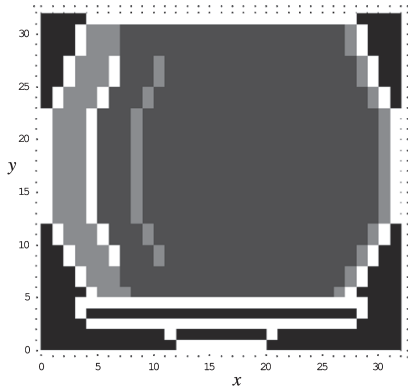

Fig. 4.2.6 The restored image with the zero-sheets of Fig. 4.2.5.

Figure 4.2.6 is the restored image that was reconstructed with the zero-sheets shown in Figs. 4.2.5 (a) and (b). The image is the same as that of Fig. 3.1. This result shows that we could judge a blur-image of the size 2×2 correctly by using the conditional expression.

As we have shown, the conditional expression of Eq. (4.2.1) is very useful and powerful tool for the Bates' blind deconvolution. Using such a conditional expression we do not have to classify the zero-values before we judge zero-values of blurs. We only connect zero-values of blurs. At present we have such a conditional expression only for blur-image of the size 2×2. It is very significant to find such conditional expressions for other blurs.

5. Enhancing a PET image by means of the Bates' blind deconvolution

We have tried deconvolution for a variety of PET images by means of the Bates' blind deconvolution. Eventually, we could succeed in finding a blur-image in a PET image. We emphasize that the result presented in this section is an invaluable result that was

achieved through tough work.

Figure 5.1 is a PET image that we downloaded from the web site http://www.cc.nih.gov/pet/images.html. It represents a set of images of human brains. Figure 5.2 exhibits an image that was extracted from Fig. 5.1. The extracted part is indicated by a white box in Fig. 5.1. The extracted image seems to be senile somehow. Our aim is to clarify whether or not any blur-images are convoluted in the extracted image. The size of the extracted image is 85 × 85, which is rather small. Therefore, it is expected that the image can be processed in a practical process time. Here, we want to mention a problem caused by extracting an image from a whole image. If the background of an extracted image is black,

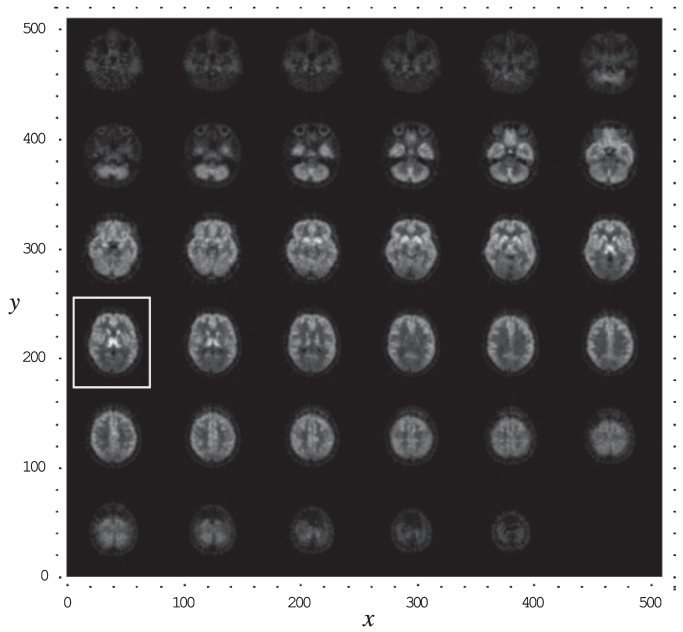

Fig. 5.1 PET images downloaded from the web site http://www.cc.nih.gov/pet/images.html.

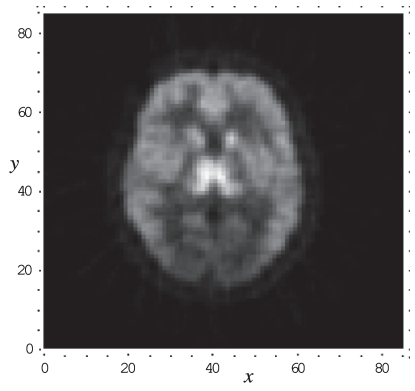

Fig. 5.2 A PET image of a human brain that was extracted from Fig. 5.1. The size of the image is 85 × 85.

no problem is caused. However, if the background of an extracted image is not black, a special technique is needed in extracting the image. In fact this is a very difficult problem. In the present case, the background of the extracted image looks black. However, actually it is not black but thick gray. This causes a severe problem in the deconvolution of the extracted image. We will return to this problem later again. Anyhow, let us now try deconvolution of the extracted image.

First we search optimal values for ρ_u and ρ_v. Figure 5.3 shows the zero-sheets of v

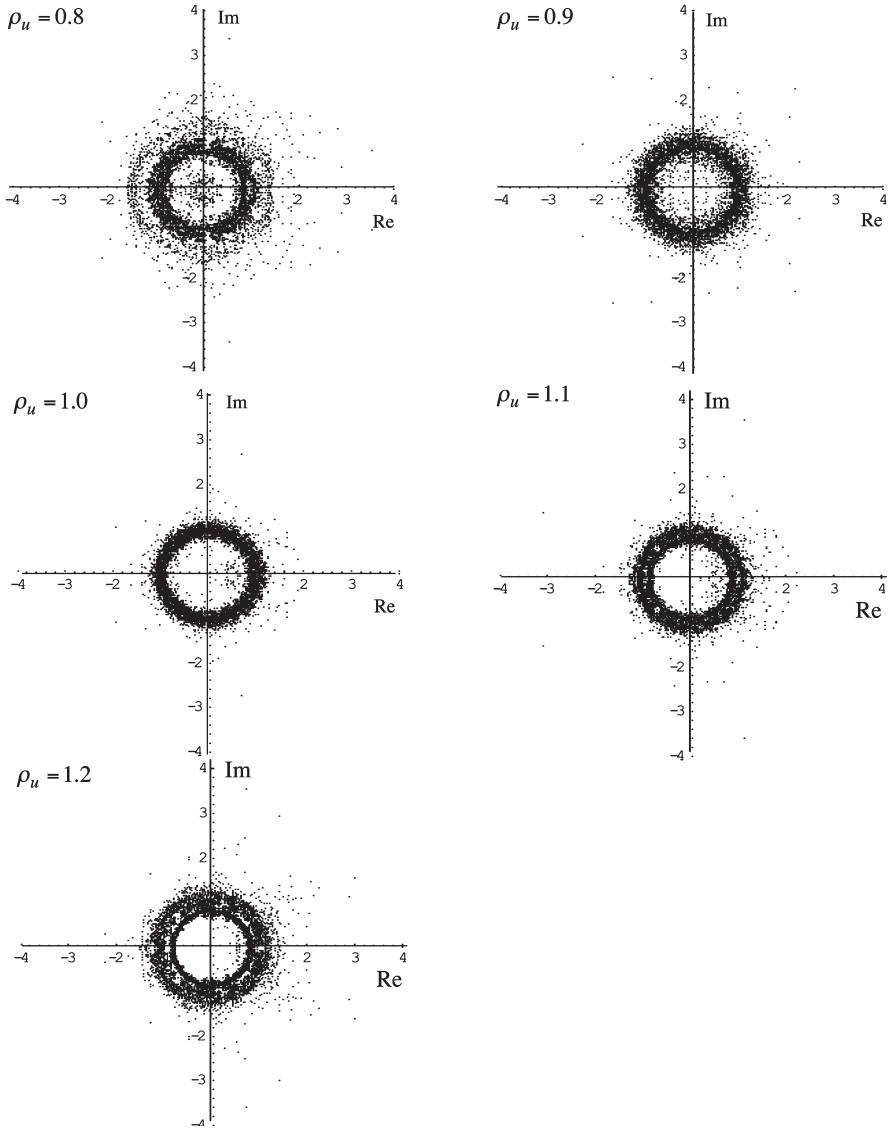

Fig. 5.3 The Zero-sheets of v for the extracted image of Fig. 5.2. The 84 β_k's are plotted for every $\Delta\phi_u = 2\pi/425$.

for various values of ρ_u. Figure 5.4 shows those for u for various ρ_v. The number of the zero-values is 84 both for v and u. In each zero-sheet shown in Figs. 5.3 and 5.4, the zero-values are plotted for every $\Delta\phi_u = 2\pi/425$ or $\Delta\phi_v = 2\pi/425$. We searched appropriate values for ρ_u and ρ_v by changing them from 0.8 to 1.2. As we have mentioned before, in order to

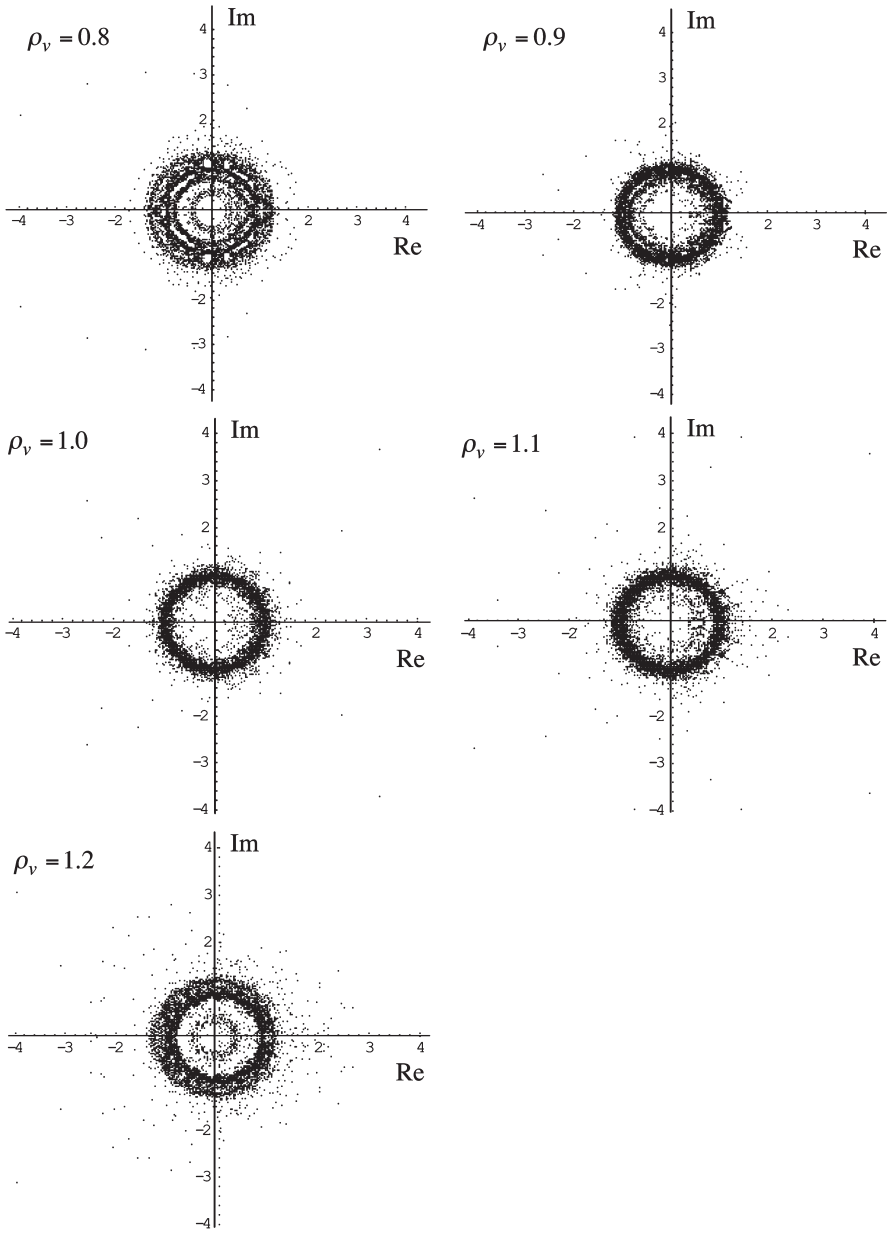

Fig. 5.4 The zero-sheets of u for the extracted image of Fig. 5.2. The 84 γ_k's are plotted for every $\Delta\phi_v = 2\pi/425$.

classify the zero-values well, we have to take ρ_u and ρ_v very different from unity. However, on the other hand, if we take ρ_u and ρ_v very different from unity, we need multi-bytes computation not to lose information of the image. Such multi-bytes computation causes explosive increase of the image processing-time. Eventually, in order to process the image in a practical processing-time we have to take ρ_u and ρ_v to be the vicinity of unity. In the present analysis we take $\rho_v = \rho_u = 1.2$ and $\rho_v = \rho_u = 0.8$.

First, we show the result of our analysis with $\rho_v = \rho_u = 1.2$. Figure 5.5 exhibits the fine structure of the zero-sheet of v for $\rho_u = 1.2$. We first tried to find blur-elements of the size 2×2 by applying the conditional expression (4.2.1) that we presented in Sec. 4. However, we could not find any blur of the size 2×2. Then, we connected each β_k from $\phi_u = 0$ to 2π and classified β_k's into groups. In connecting each β_k we used the differential equation (4.1.1) that we presented in Sec. 4. In this case, the 84 β_k's were classified into 6 groups. Figure 5.6 shows the classified β_k's.

The results of the classification of β_k's shown in Fig. 5.6 imply that the size of x-space of the smallest image is 3. As we mentioned above, we found no blur of the size 2×2 by using the conditional expression of Eq. (4.2.1). This is consistent with the results of the classification of β_k's. Next, we judge zero-sheets of blurs. A key point in judging burs would be the size of image elements. If an image element is small enough, it may be a candidate for blurs. In Fig. 5.6, Group-4, -5 and -6 represent small images. Therefore, we tried deconvolution by regarding those three groups as the candidates for blurs. We reconstructed images by removing each one of the three candidates. The results are shown in Fig. 5.7. The reconstructed images are quite different from the observed image of Fig. 5.2. We further tried to reconstruct images by removing two of the three candidates. However, we could not obtain any plausible images. Thus, zero-values of Group-4, -5 and -6 cannot be regarded as those of blur-images.

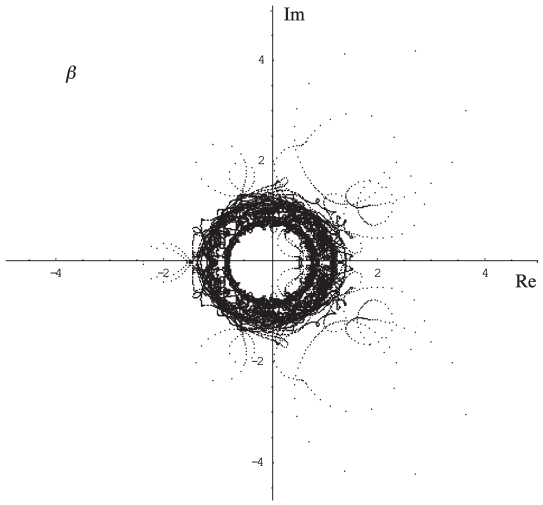

Fig. 5.5 The fine structure of the zero-sheet of v for $\rho_u = 1.2$.

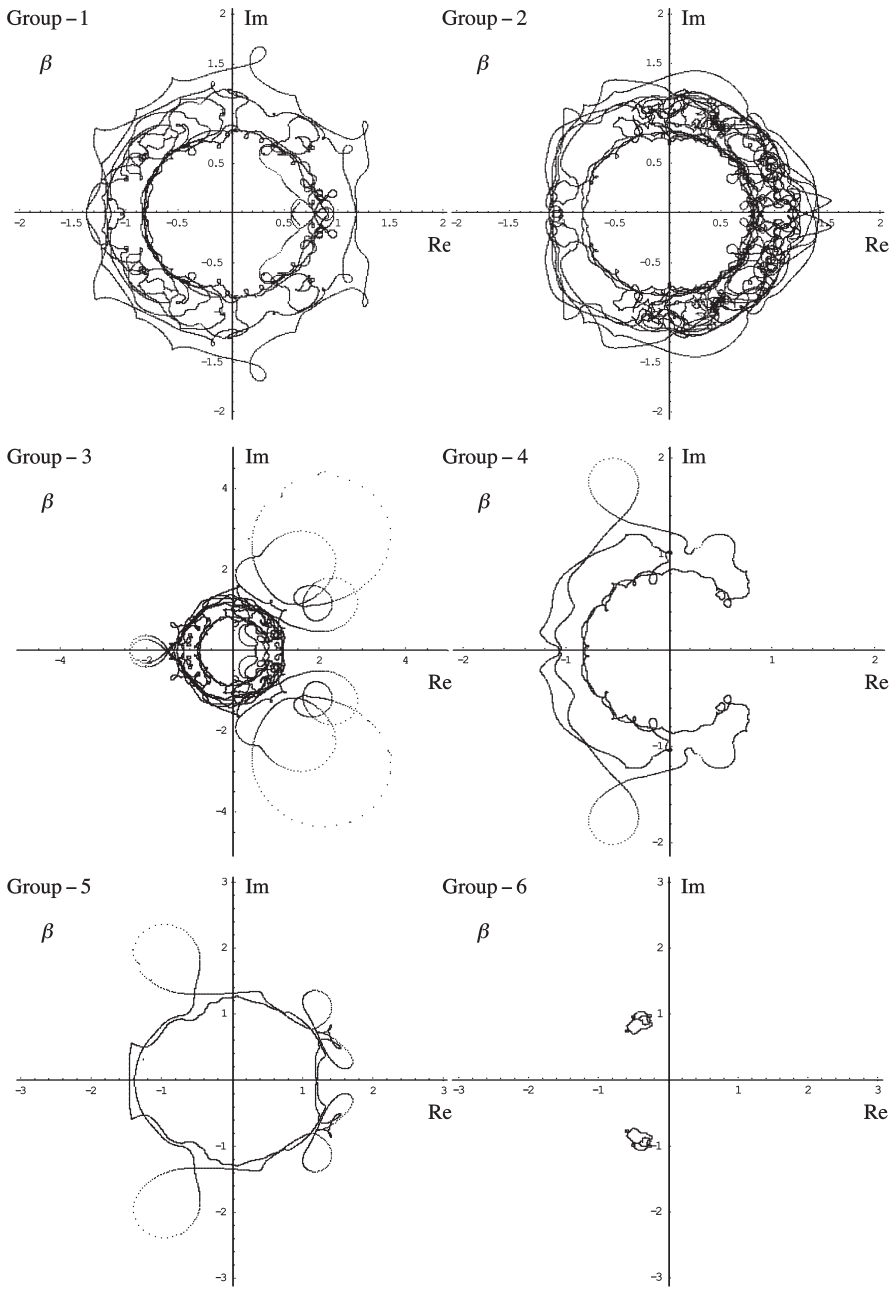

Fig. 5.6 The classified β_k's. Group-1 consists of 20 β_k's. Group-2 consists of 32 β_k's. Group-3 consists of 22 β_k's. Group-4 consists of 5 β_k's. Group-5 consists of 3 β_k's. Group-6 consists of 2 β_k's.

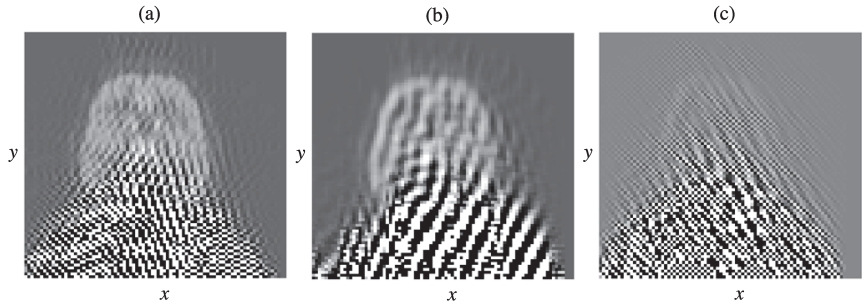

Fig. 5.7 (a) The image reconstructed by removing β_k's of Group-6. (b) The image reconstructed by removing β_k's of Group-5. (c) The image reconstructed by removing β_k's of Group-4.

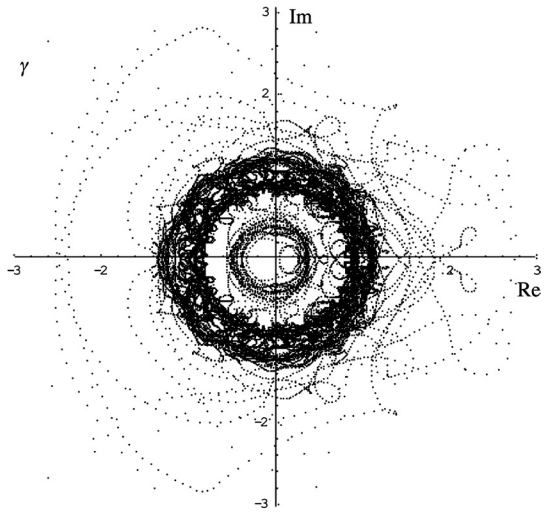

Fig. 5.8 The fine structure of the zero-sheet of u for $\rho_v = 1.2$.

Next, we examine the zero-sheets of u. Figure 5.8 exhibits the fine structure of the zero-sheet of u for $\rho_v = 1.2$. We could classify 84 γ_k's into four groups by connecting each γ_k from ϕ_v=0 to 2π. Figure 5.9 shows the results. The results of the classification indicate that the smallest image element is of Group-4 that consists of 7 γ_k's. Therefore, it is expected that a blur must be an image of the size 8 × 8 or larger. Anyhow, we tried to reconstruct an image by removing γ_k's of Group-4. Figure 5.10 shows the result. The reconstructed image is quite different from the observed image of Fig. 5.2. Eventually, we failed in restoring the image of Fig. 5.2 with the zero-sheets for $\rho_u = \rho_v = 1.2$. There are two reasons for this: (1) the values of ρ_v and ρ_u are not appropriate, (2) any blurs are not originally convoluted.

Then, we reanalyzed with $\rho_u = \rho_v = 0.8$. Figure 5.11 shows the fine structure of the zero-sheet of v for $\rho_u = 0.8$. Figure 5.12 exhibits β_k's classified by the differential equation (4.1.1). The 84 β_k's are classified into 6 groups well.

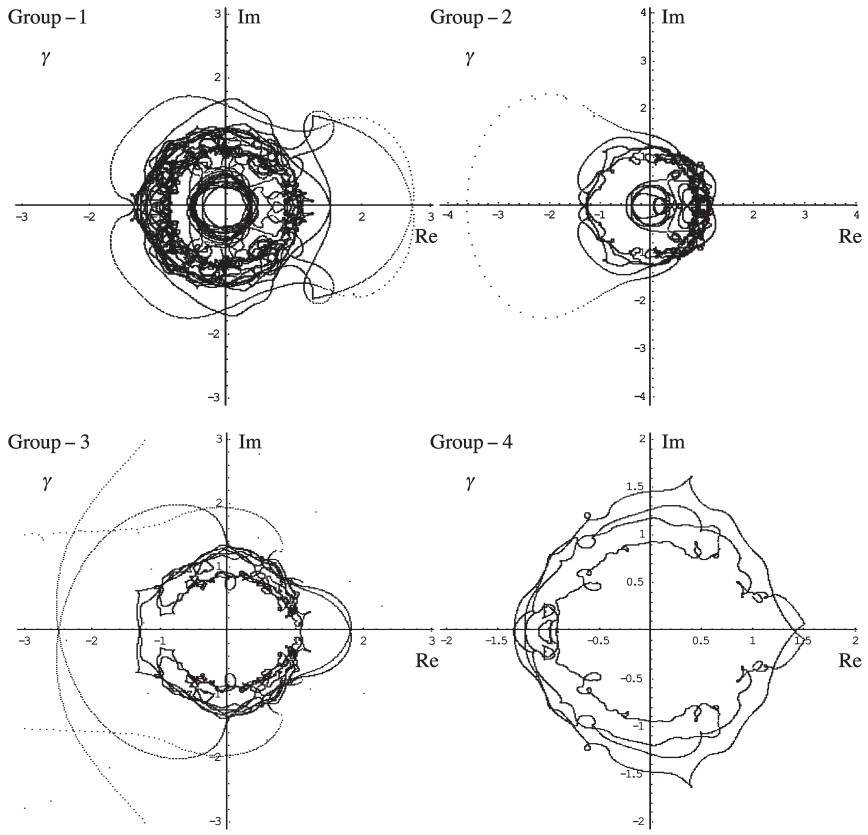

Fig. 5.9 The classified γ_k's of u with $\rho_v = 1.2$. Group-1 consists of 41 γ_k's. Group-2 consists of 18 γ_k's. Group-3 consists of 18 γ_k's. Group-4 consists of 7 γ_k's.

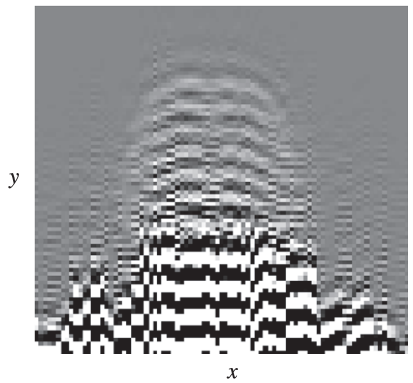

Fig. 5.10 The image reconstructed by removing γ_k's of Group-4.

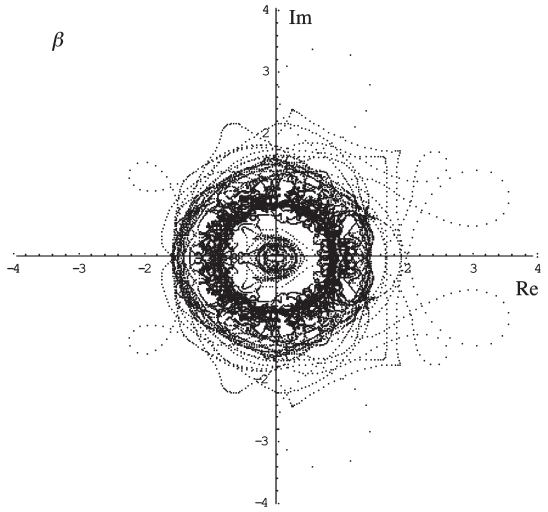

Fig. 5.11 The fine structure of the zero-sheet of v for $\rho_u = 0.8$.

As seen in the figure, the group-4, -5 and -6 represent small image-elements. In Figure 5.13 we show images that we reconstructed by removing β_k's of each one of the Group-4, -5 and -6. They are all quite different from the observed image of Fig. 5.2, as in the case of $\rho_u = 1.2$. We also tried to reconstruct images by removing two of the three groups. However, we could not obtain any plausible images, as in the case of $\rho_u = 1.2$.

Next we examine the zero-sheet of u. Figure 5.14 exhibits the fine structure of the zero-sheet of u for $\rho_v = 0.8$. The classified γ_k's of u are shown in Fig. 5.15. In this case, 84 γ_k's are classified into 6 groups by the differential equation (4.1.1).

As seen in Fig. 5.15, Group-5 and -6 imply the smallest image elements. We reconstructed an image by removing the zero-values of Group-6. Figure 5.16 shows the reconstructed image. The reconstructed image is very similar to the observed image of Fig. 5.2. In the reconstructed image the light and shade of the image looks enhanced compared to those of the original image. Figure 5.17 (a) exhibits the difference in the brightness between the enhanced image and the observed image. In Fig. 5.17 (b), the difference in the brightness of the 44th row is shown. It is noted that in some parts the difference in the brightness is amplified. Thus, we are convinced that a blur was surely excluded and the observed image is restored certainly.

Although we are convinced that the image of Fig. 5.16 is correctly restored, we are anxious somehow about the irregularity of the restored image. We obtained the observed image of Fig. 5.2 by extracting it from the whole image of Fig. 5.1. The background of the extracted image looks black. However, as we mentioned before, in fact the background is not black but thick gray. We guess that this causes such irregularity in the restored image. Then, we made a modification on the extracted image of Fig. 5.2. We applied a suppress function (or window function) to the extracted image. The suppress function adjusts smoothly the brightness of the image to zero in the vicinity of the edge of the extracted

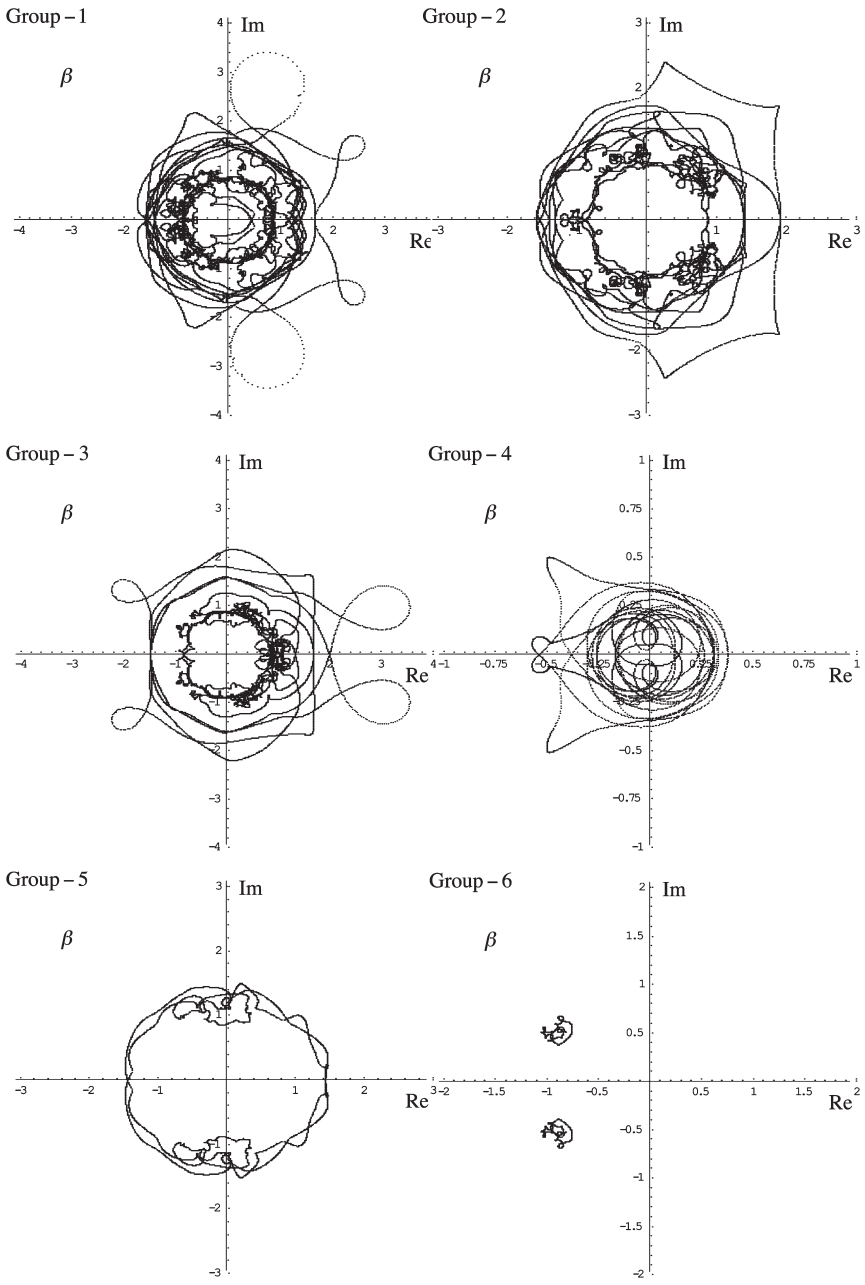

Fig. 5.12 The zero-values β_k's classified with $\rho_u = 0.8$. Group-1 consists of 31 β_k's. Group-2 consists of 23 β_k's. Group-3 consists of 22 β_k's. Group-4 consists of 2 β_k's. Group-5 consists of 4 β_k's. Group-6 consists of 2 β_k's.

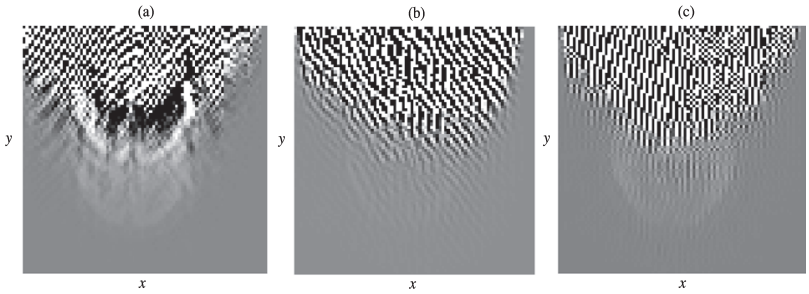

Fig. 5.13 (a) The image reconstructed by removing β_k's of Group-4. (b) The image reconstructed by removing β_k's of Group-5. (c) The image reconstructed by removing β_k's of Group-6.

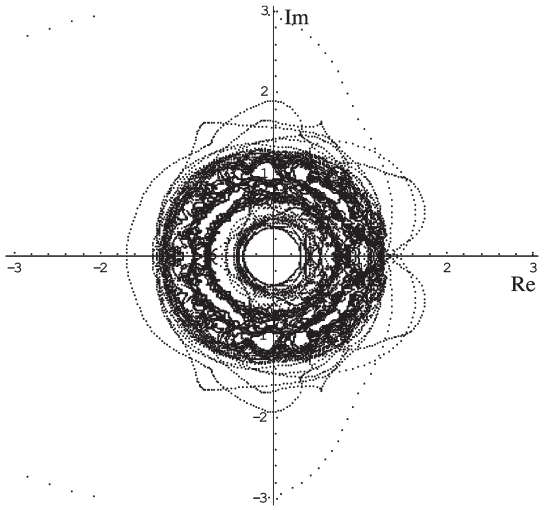

Fig. 5.14 The fine structure of the zero-sheet of u for $\rho_v = 0.8$.

image. We carried out the image processing for such a modified image, in the same way as we did for the extracted image. We show the result in Fig. 5.18 (a). Apparently, the irregularity seen in Fig. 5.16 has disappeared in the restored image of Fig. 5.18 (a). Figure 5.18 (b) shows the difference in the brightness of the 44th row between the restored and the original images. In some parts the difference in the brightness is certainly amplified. The result of this analysis indicates that for the blind deconvolution of PET images it is important to establish a versatile technique for extracting an image from a whole image.

To the end of this section, we mention the blur image that we removed from the observed image. We could find a blur-element in u-space. The blur-element consists of two zero-values. This means that the size of the blur-element in x-space is three. The zero-sheet of the blur-element in u-space is shown in Fig. 5.15, i.e., Group-6. The zero-values of Group-6 have apparently ϕ_v dependences. This implies that the size of the blur-element in y-space is larger than two. If the size of the blur-element in y-space is one, then the zero-values of

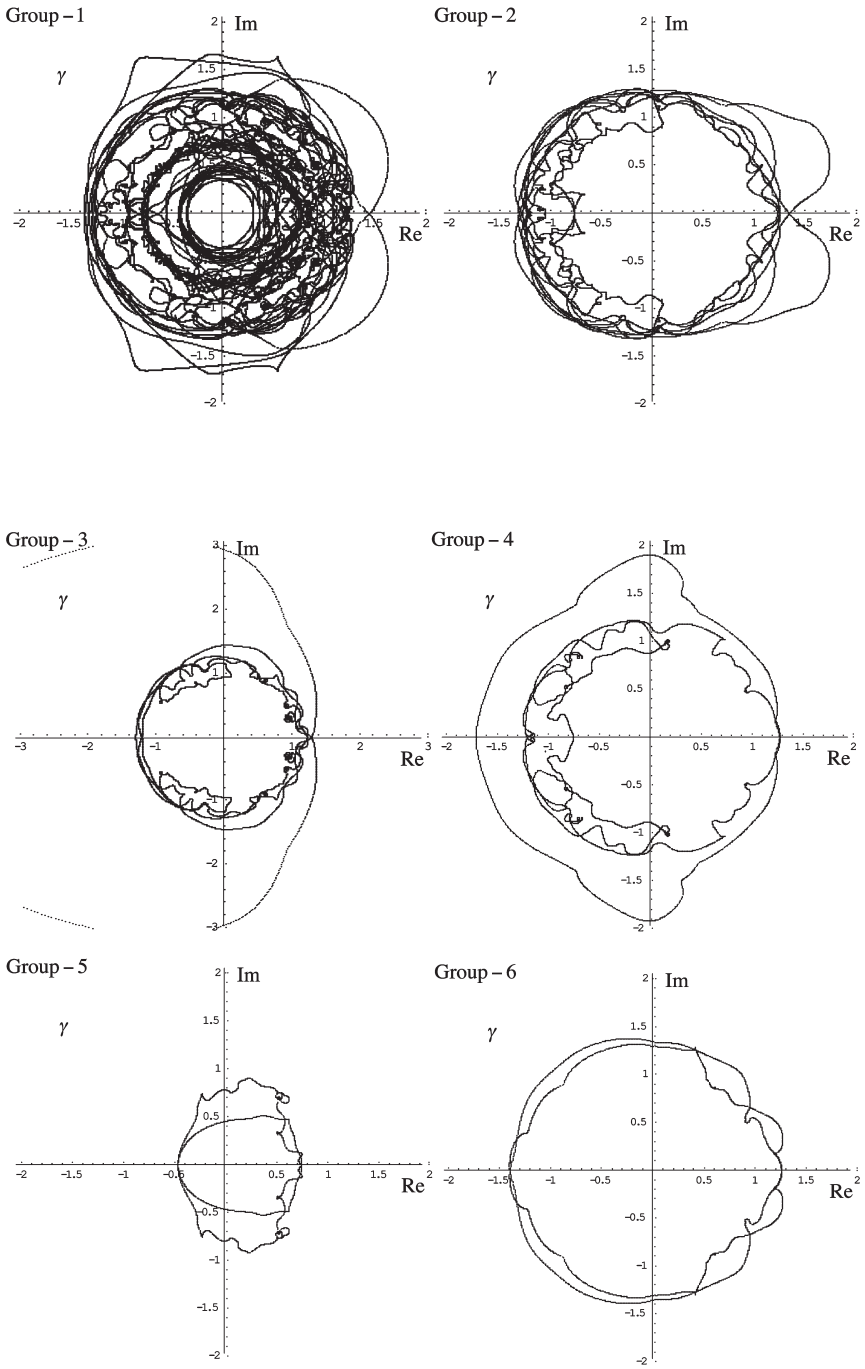

Fig. 5.15 The classified γ_k's for $\rho_v = 0.8$. Group-1 consists of 52 γ_k's. Group-2 consists of 13 γ_k's. Group-3 consists of 8 γ_k's. Group-4 consists of 7 γ_k's. Group-5 consists of 2 γ_k's. Group-6 consists of 2 γ_k's.

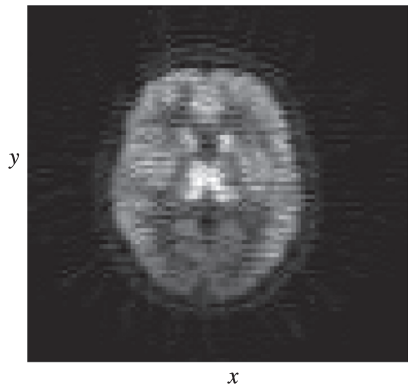

Fig. 5.16 An image reconstructed by removing γ_k's of Group-6.

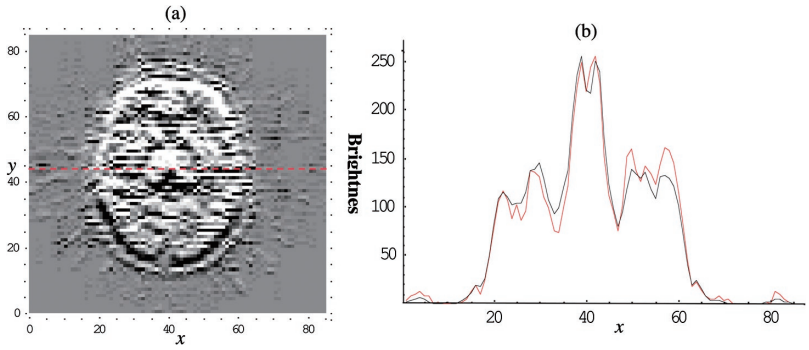

Fig. 5.17 (a) The difference in the brightness between the enhanced and the observed images. (b) The brightness of the 44th row that was extracted from Fig. 5.15 (a). The red and black lines indicate the brightness of the enhanced image and the observed image, respectively.

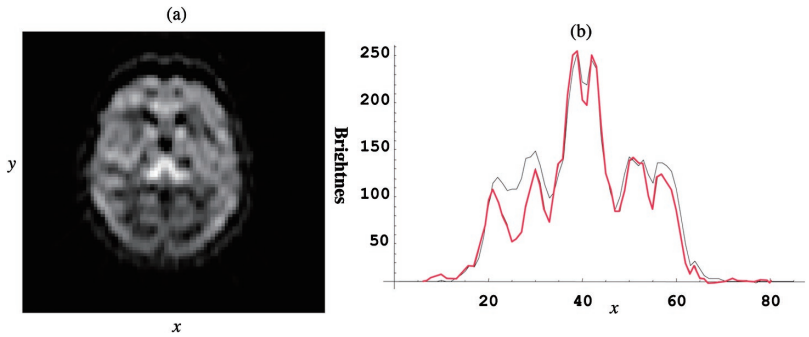

Fig. 5.18 (a) The image restored from the extracted image to which a suppress function was applied. (b) The red and black lines respectively indicate the brightness of the restored image and extracted image to which a suppress function was applied.

u do not have any ϕ_v dependence. Hence, we can guess that the blur-element is of $3 \times n$ ($n \geq 2$). However, we did not find any blur-element in v-space. This is a puzzle. At present, we do not have any answer to this inconsistency. We are now reanalyzing this problem.

6. Summary

We examined Bates' blind deconvolution to apply it to the restoration of PET images. An essential problem in the Bates' method is how we separate zero-sheets of blur-images from those of original (observed) images. If given images are simple and small enough, we do not need any special technique to extract the zero-sheets of blur-images. In actual images like PET images, however, the structure of the their zero-sheets is complicated and their image-sizes are large. Therefore, we need a special method to extract the zero-sheets of blur-images from the whole zero-sheet. In the present work, we developed a method to achieve this. In our method, first we solve the zero-values of a given image at discrete points of phase parameters, in a desired accuracy. We carry out this by *Mathematica*. Next, we classify the zero-values into groups by relating each of the zero-values obtained at different points of the phase parameters. We perform this by means of differential equations for the zero-values. We solve the differential equations by *Fortran* in quadruple precision. This method is very powerful and enables us to process actual images in a practical processing time. In this sense, our method is practical.

Our method summarized above is very powerful but somewhat tedious. If we can judge the zero-values of any blur-images without classifying the zero-values, it would simplify the image processing greatly. In the present work, we showed that such a method is possible in principle if blur-images are those of the size 2×2. We derived a conditional expression for such blur-images. By using the conditional expression we can judge blur-images of the size 2×2 almost automatically. We are now trying to find such conditional expressions for other types of blur-images.

We succeeded in restoring an actual PET image using our methods summarized above. The restored image is surely enhanced compared with the observed PET image. This verifies that our methods are very useful in applying the Bates' blind deconvolution to the restoration of PET images. In conclusion, it is possible to improve the resolution of PET images by an image restoration processing. We are now trying to develop an advanced image-processing system by which we can restore observed PET images almost automatically.

Acknowledgments

We would like to thank Dr. Tanaka at RIKEN for his informative suggestions. One of the authors Okano would like to thank Prof. Kurozumi at Department of Information and Communication Sciences, Kyoto Sangyo University for his useful discussion. This work has been supported by the Grant-in-Aid for Scientific Research 15650107 from Japan Society for the Promotion of Science, the Science Research Promotion Fund from the Promo-

tion and Mutual Aid Corporation for private Schools of Japan, and a grant from Institute for Comprehensive Research, Kyoto-Sangyo University.

References

1) 田中栄一, "PET の現状と将来", RADIOISOTOPES, **46**, 733–742 (1997)；村山秀雄, "ポジトロン・エミッション・トモグラフィ（PET)", 放射線, **24**(2), 366–371（2000）；日本核医学会（編), PET 検査 Q&A（2000）；日本核医学会（編), 核医学検査 Q&A（1997）；村山秀雄, "立体計測型ポジトロン断層撮像法における画像再構成", 光学, **29**, 366–371（2000）；村山秀雄, "PET の放射線検出系", Med. Imag. Tech., **18**, 15–23（2000).
2) R. C. Gonzalez and R. E. Woods, "Digital Image Processing Second Edition", Prentice Hall, 116–140, 2002.
3) R. C. Gonzalez and R. E. Woods, "Digital Image Processing Second Edition", Prentice Hall, 148–213, 2002.
4) R. G. Lane and R. H. T. Bates, "Automatic multidimentional deconvolution", J. Opt. Soc. Am. A, **4**, 180–188 (1987).
5) 南　茂夫, 河田　聡, "科学計測のためのデータ処理入門", 93–119, 2002.